

# THE ANTARCTIC SUBMILLIMETER TELESCOPE AND REMOTE OBSERVATORY (AST/RO)

Antony A. Stark<sup>1,7</sup>, John Bally<sup>2,7</sup>, Simon P. Balm<sup>1</sup>, T. M. Bania<sup>3</sup>, Alberto D. Bolatto<sup>3</sup>,  
Richard A. Chamberlin<sup>3,4</sup>, Gregory Engargiola<sup>5,6</sup>, Maohai Huang<sup>3</sup>, James G. Ingalls<sup>3,9</sup>,  
Karl Jacobs<sup>8</sup>, James M. Jackson<sup>3</sup>, Jacob W. Kooi<sup>9</sup>, Adair P. Lane<sup>1</sup>, K.-Y. Lo<sup>5</sup>, Rodney D.  
Marks<sup>1</sup>, Christopher L. Martin<sup>1</sup>, Dennis Mumma<sup>7</sup>, Roopesh Ojha<sup>1</sup>, Rudolf Schieder<sup>8</sup>,  
Johannes Staguhn<sup>8,10</sup>, Jürgen Stutzki<sup>8</sup>, Christopher K. Walker<sup>11</sup>, Robert W. Wilson<sup>1,7</sup>,  
Gregory A. Wright<sup>6</sup>, Xiaolei Zhang<sup>1,10</sup>, Peter Zimmermann<sup>12</sup>, and Rüdiger Zimmermann<sup>12</sup>

The Center for Astrophysical Research in Antarctica

Received \_\_\_\_\_; accepted \_\_\_\_\_

Submitted to the *Astrophysical Journal*, 16 August 2000

---

<sup>1</sup>Harvard-Smithsonian Center for Astrophysics; 60 Garden St.; Cambridge, MA 02138  
(aas, adair, cmartin@cfa.harvard.edu).

<sup>2</sup>CASA; University of Colorado; Boulder, CO 80309.

<sup>3</sup>Boston University; 725 Commonwealth Ave.; Boston, MA 02215.

<sup>4</sup>Caltech Submillimeter Observatory; 111 Nowelo St.; Hilo, HI 96720.

<sup>5</sup>University of Illinois; 1002 W. Green St.; Urbana, IL 61801.

<sup>6</sup>Radio Astronomy Lab; University of California; Berkeley, CA 94720  
(greg@astron.berkeley.edu).

<sup>7</sup>Bell Laboratories; 791 Holmdel-Keyport Rd.; Holmdel, NJ 07733.

<sup>8</sup>I. Physikalisches Institut, Universität zu Köln; Zülpicher Straße 77; D-50937 Köln, Germany.

<sup>9</sup>California Institute of Technology; Pasadena, CA 91125.

<sup>10</sup>NASA GSFC; Code 685; Greenbelt, MD 20771 (staguhn, zhang@stars.gsfc.nasa.gov).

<sup>11</sup>Steward Observatory; 933 N. Cherry Ave.; University of Arizona; Tucson, AZ 85721.

<sup>12</sup>Radiometer Physics GmbH; Birkenmaarsestrasse 10; 53340 Meckenheim, Germany.

## ABSTRACT

AST/RO, a 1.7 m diameter telescope for astronomy and aeronomy studies at wavelengths between 200 and 2000  $\mu\text{m}$ , was installed at the South Pole during the 1994-95 Austral summer. The telescope operates continuously through the Austral winter, and is being used primarily for spectroscopic studies of neutral atomic carbon and carbon monoxide in the interstellar medium of the Milky Way and the Magellanic Clouds. The South Pole environment is unique among observatory sites for unusually low wind speeds, low absolute humidity, and the consistent clarity of the submillimeter sky. Four heterodyne receivers and three acousto-optical spectrometers are installed. Telescope pointing, focus, and calibration methods as well as the unique working environment and logistical requirements of the South Pole are described.

*Subject headings:* atmospheric effects—instrumentation: detectors—radio lines: general—site testing—submillimeter—telescopes

## 1. Introduction

Very little of the submillimeter-wave radiation from astronomical sources reaches the Earth's surface; this means that ground-based submillimeter-wave astronomy is hampered by skies which are usually opaque. Astronomers have therefore sought high, arid sites for new submillimeter telescopes, to find better transparency and reduced sky noise. Among the most promising sites for submillimeter-wave astronomy is the South Pole, an exceptionally dry and cold site which has unique logistical opportunities and challenges.

In the past decade, a year-round observatory has been established at the Pole by the Center for Astrophysical Research in Antarctica (CARA), an NSF Science and

Technology Center. CARA has fielded several major telescope facilities: AST/RO (the Antarctic Submillimeter Telescope and Remote Observatory, a 1.7-m telescope (see Figure 1), Python and Viper (Cosmic Microwave Background experiments), DASI (the Degree-Angular Scale Interferometer), and SPIREX (the South Pole Infrared Explorer, a 60-cm telescope, now decommissioned). These facilities are conducting site characterization and astronomical investigations from millimeter wavelengths to the near-infrared (Novak & Landsberg 1998, see also URL <http://astro.uchicago.edu/cara>). AST/RO was installed at the Pole in Austral summer 1994-1995 (Lane & Stark 1996), and was the first submillimeter-wave telescope to operate on the Antarctic Plateau in winter. AST/RO is designed for astronomy and aeronomy with heterodyne and bolometric detectors at wavelengths between 3 mm and  $200\mu\text{m}$ . An up-to-date list of scientific publications and technical memoranda from AST/RO may be found at the observatory website at <http://cfa-www.harvard.edu/~adair/AST-RO>. Observing time on AST/RO is now open to proposals from the worldwide astronomical community.

This paper describes observing operations at AST/RO. A summary of logistical support requirements and measured site characteristics is given in §2. The instrument and observatory facilities are described in §3 and in Stark et al. (1997). Telescope pointing, calibration, and observing methods are described in §4.

## 2. Site Characteristics

### 2.1. Logistics

The AST/RO telescope is located in the *Dark Sector* of the United States National Science Foundation Amundsen-Scott South Pole Station. The station provides logistical support for the observatory: room and board for on-site scientific staff, electrical power,

network and telephone connections, heavy equipment support, and cargo and personnel transport. The station powerplant provides about 25 kW of power to the AST/RO building out of a total generating capacity of about 490 kW. The South Pole has been continuously populated since the first station was built in November 1956. The current station was built in 1975, and new structures have been added in subsequent years to bring the housing capacity to 210 people in Austral summer and 45 in the Austral winter. New station facilities are under construction and are expected to be operational by 2005. These include living quarters for a winter-over staff of 50, a new powerplant with greater generating capacity, and a new laboratory building.

Heavy equipment at South Pole Station includes cranes, forklifts, and bulldozers; these can be requisitioned for scientific use as needed. The station is supplied by over 200 flights each year of LC130 ski-equipped cargo aircraft. Annual cargo capacity is about 3500 tons. Aircraft flights are scheduled from late October to early-February so that the station is inaccessible for as long as nine months of the year. This long *winter-over* period is central to all logistical planning for Polar operations.

The SIS receivers used on AST/RO each require about 2 liters of liquid helium per day. As of mid-2000, total usage of liquid helium at the Pole averages 30 liters per day for all experiments. One or two helium-filled weather balloons are launched each day. There is an ongoing loss of helium from the station, as it is used for a variety of experiments. The National Science Foundation and its contractors must supply helium to the Pole, and the most efficient way to transport and supply helium is in liquid form. Before the winter-over period, one or more large (4000 to 12000 liter) storage dewars are brought to the Pole for winter use; some years this supply lasts the entire winter, but in 1996 and 2000 it did not. In December 1998, no helium was available during a period scheduled for engineering tests, resulting in instrumental problems for AST/RO during the subsequent winter. The supply

of liquid helium has been a chronic problem for AST/RO and for South Pole astronomy, but improved facilities in the new station should substantially improve its reliability.

Internet and telephone service to the Pole is provided by a combination of two low-bandwidth satellites, LES-9 and GOES-3, and the high-bandwidth (3 Mbps) NASA Tracking and Data Relay Satellite System TDRS-F1. These satellites are geosynchronous but not geostationary, since the orbits are inclined. Geostationary satellites are always below the horizon and cannot be used. Internet service is intermittent through each 24-hour period because each satellite is visible only during the southernmost part of its orbit; the combination of the three satellites provides an Internet connection for approximately 12 hours within the period 1–16 hr Greenwich LST. The TDRS link helps provide a store-and-forward automatic transfer service for large computer files. The total data communications capability is about 5 Gbytes per day. AST/RO typically generates 1–2 Mbytes per day. Additional voice communications are provided by a fourth satellite, ATS-3, and high frequency radio.

On AST/RO, all engineering operations for equipment installation and maintenance are tied to the annual cycle of physical access to the instrument. Plans and schedules are made in March and April for each year's deployment to the Pole: personnel on-site, tasks to be completed, tools and equipment needed. All equipment must be ready for shipment by the end of September. Orders for new equipment should be complete by June and new equipment should be tested and ready to ship by August. AST/RO group members deploy to the Pole in groups of two to six people throughout the Austral summer season, carry out their planned tasks as well as circumstances allow, and return, after stays ranging from 2 weeks to 3 months. Each year there is an AST/RO *winter-over scientist*, a single person who remains with the telescope for one year. The winter-over scientist position is designed to last three years: one year of preparation and training, one year at the Pole

with the telescope, and one year after the winter-over year to reduce data and prepare scientific results. If there are no instrumental difficulties, the winter-over scientist controls telescope observations through the automated control program *OBS*, carries out routine pointing and calibration tasks, tunes the receivers, and fills the liquid helium dewars. If instrumental difficulties develop, the winter-over scientist carries out repairs in consultation with AST/RO staff back at their home institutions and with the help of other winter-over staff at the Pole.

AST/RO is located on the roof of a dedicated support building across the aircraft skiway in the *Dark Sector*, a grouping of observatory buildings in an area designated to have low radio emissions and light pollution. The AST/RO building is a single story, 4m × 20m, and is elevated 3m above the surface on steel columns to reduce snow drifts. The interior is partitioned into six rooms, including laboratory and computer space, storage areas, a telescope control room, and a Coudé room containing the receivers on a large optical table directly under the telescope.

## 2.2. Instrument Reliability

AST/RO is a prototype, the first submillimeter-wave telescope to operate year-round on the Antarctic plateau. As such, its operation is in part an experiment, intended to demonstrate feasibility and to identify areas of difficulty. A unique challenge of South Pole operations is the lack of transport for personnel and equipment during the nine month winter-over period. Spare or replacement parts for most of the critical system assemblies have been obtained, shipped to Pole, and stored in the AST/RO building. In a typical year, failure occurs in two or three system subassemblies, such as a drive system power supply or a submillimeter-wave local oscillator chain. Usually a repair or work-around is effected by the winter-over scientist. There are, however, single points of failure which can cause the



Fig. 1.— **AST/RO at South Pole.** The Antarctic Submillimeter Telescope and Remote Observatory atop its building at the South Pole in February 1997. Standing next to the telescope are G. Wright of Bell Labs, and X. Zhang and A. Stark of SAO. The telescope rests on a steel support tower which is structurally isolated from the building, and can be covered by a fold-off canopy made of canvas and aluminum tubing. An LC130 cargo aircraft is parked on the skiway. The South Pole itself is slightly below and to the right of the tail of the airplane. (photo credit: A. Lane)



cessation of observatory operations until the end of the winter. Between 1995 and 2000, observations or engineering tests were planned for a total of 54 months, of which about half were successful. The most important cause of telescope downtime has been incapacitation, either physical or mental, of the winter-over scientist, resulting in 14 months of lost time. Failure of the liquid helium supply was responsible for a further 11 months of lost time. In future, both of these causes for failure will be substantially reduced. Starting in 2002, it is planned that AST/RO will field two winter-over scientists. Beginning in 2003, the completion of a new liquid helium supply facility as part of the new South Pole Station Modernization plan will eliminate single points of failure for the liquid helium supply.

### 2.3. Site Testing

The sky is opaque to submillimeter wavelengths at most observatory sites. Submillimeter astronomy can only be pursued from dry, frigid sites, where the atmosphere contains less than 1 mm of precipitable water vapor (PWV). Water vapor is usually the dominant source of opacity, but thousands of other molecular lines contribute (Waters 1976; Bally 1989) a *dry air* component to the opacity. Chamberlin & Bally (1995), Chamberlin et al. (1997), and Chamberlin (2000) showed that the dry air opacity is relatively more important at the Pole than at other sites. Dry air opacity is less variable than the opacity caused by water vapor, and therefore causes less *sky noise*. Of all ground-based observatory sites that have been tested for submillimeter-wave sky quality, the best results have come from the Amundsen-Scott South Pole Station (Lane 1998).

Physical parameters of the South Pole site of AST/RO are given in Table 1. The South Pole meteorology office has used balloon-borne radiosondes to measure profiles above the Pole of temperature, pressure, and water vapor at least once a day for several decades (Schwerdtfeger 1984). These have typically shown atmospheric water vapor values about

90% of saturation for air at the observed temperature and pressure. The precipitable water vapor (PWV) values consistent with saturation are, however, extremely low because the air is dessicated by the frigid temperatures. Judging by other measures of PWV such as LIDAR and mid-infrared spectroscopy, the calibration of the hygrometers used on balloon sondes was accurate between 1991 and 1996. On February 22, 1997, the balloon radiosonde type was changed from an A.I.R. Model 4a to the A. I. R. Model 5a, and the average PWV values indicated by the new radiosondes dropped by 70% (see Figure 2); these new values appear to be spuriously low. A firm upper limit to the PWV can be set by calculating what the PWV would be if the column of air were 100% saturated with water vapor at the observed temperature and pressure, the *saturation-point PWV*. Since the temperature and pressure measurements from balloon sondes are accurate, and since the atmosphere cannot be significantly supersaturated, the saturation-point PWV is a reliable upper limit to the true PWV. Values of the saturation-point PWV for a 38 year period are shown in Figure 3 (Chamberlin 2000). Figure 4 shows the PWV for each day of the year averaged over all the years in this data set to show the average seasonal variation in the water vapor content of the atmosphere. *PWV values at the Pole are small, stable, and well-understood.*

Quartile values of the distribution of PWV with time are plotted in Figure 5 (from Lane 1998), where they are compared with corresponding values for Mauna Kea and for the proposed ALMA site at Chajnantor. The relation between PWV and measured opacity at 225 GHz (Hogg 1992; Masson 1994, S. Foster, private communication) was used to derive the PWV values for Mauna Kea and Chajnantor. The data are separated into the best 6-month period and the remainder of the year. Of the three sites, South Pole has by far the lowest PWV, during Austral summer as well as winter.

Millimeter and submillimeter-wave atmospheric opacity at the South Pole has been measured using skydip techniques. Chamberlin et al. (1997) made over 1100 skydip

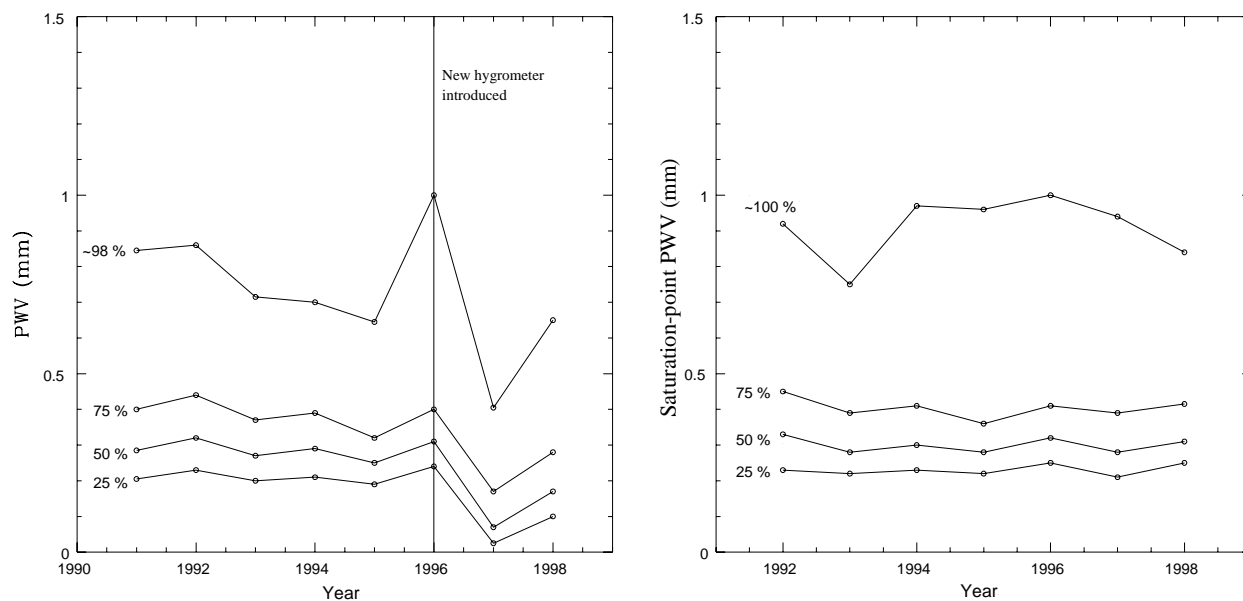


Fig. 2.— **Balloon Measurements of PWV at Pole.** (left) Quartiles of precipitable water vapor (PWV) distribution in winter (day-of-year 100–300) from 1991 through 1998, calculated from balloon-borne radiosonde measurements. The radiosonde type was changed in 1996, and the subsequent calibration has been spurious. This new radiosonde, the AIR model 5a, has been used in measurements at other sites, in particular the peaks surrounding Chajnantor plateau (Giovannelli et al. 1999); the 1997 Pole measurements make possible a direct comparison. (right) Quartiles of saturation-point PWV distribution in winter (day-of-year 100-300) from 1992 through 1998, calculated from balloon-borne pressure and temperature measurements. Saturation-point PWV is calculated by assuming 100% water vapor saturation for a column of air with a measured temperature and pressure profile. Since temperature and pressure sensor calibration is more reliable than hygrometer calibration, this value gives reproducible results. If hygrometer measurements from 1991-1996 can be trusted, the winter South Pole atmosphere is, on average, 90% saturated.

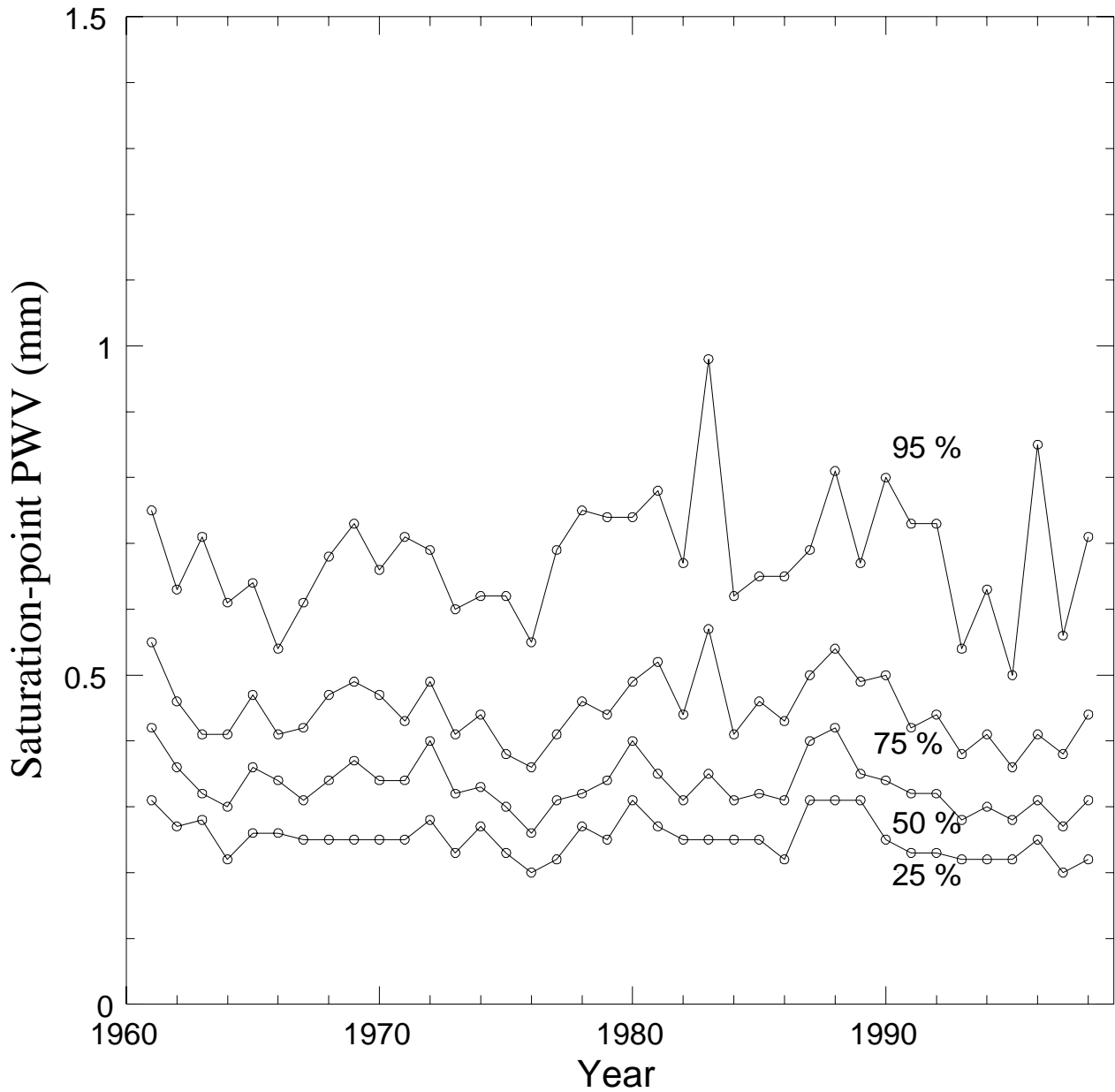


Fig. 3.— Saturation-point PWV at Pole, 1961-1998, adapted from Chamberlin (2000). Quartiles of saturation-point PWV distribution during the winter (day-of-year 100-300) for 1961 through 1998, calculated from balloon-borne pressure and temperature measurements. This figure illustrates the long-term stability of the South Pole climate.

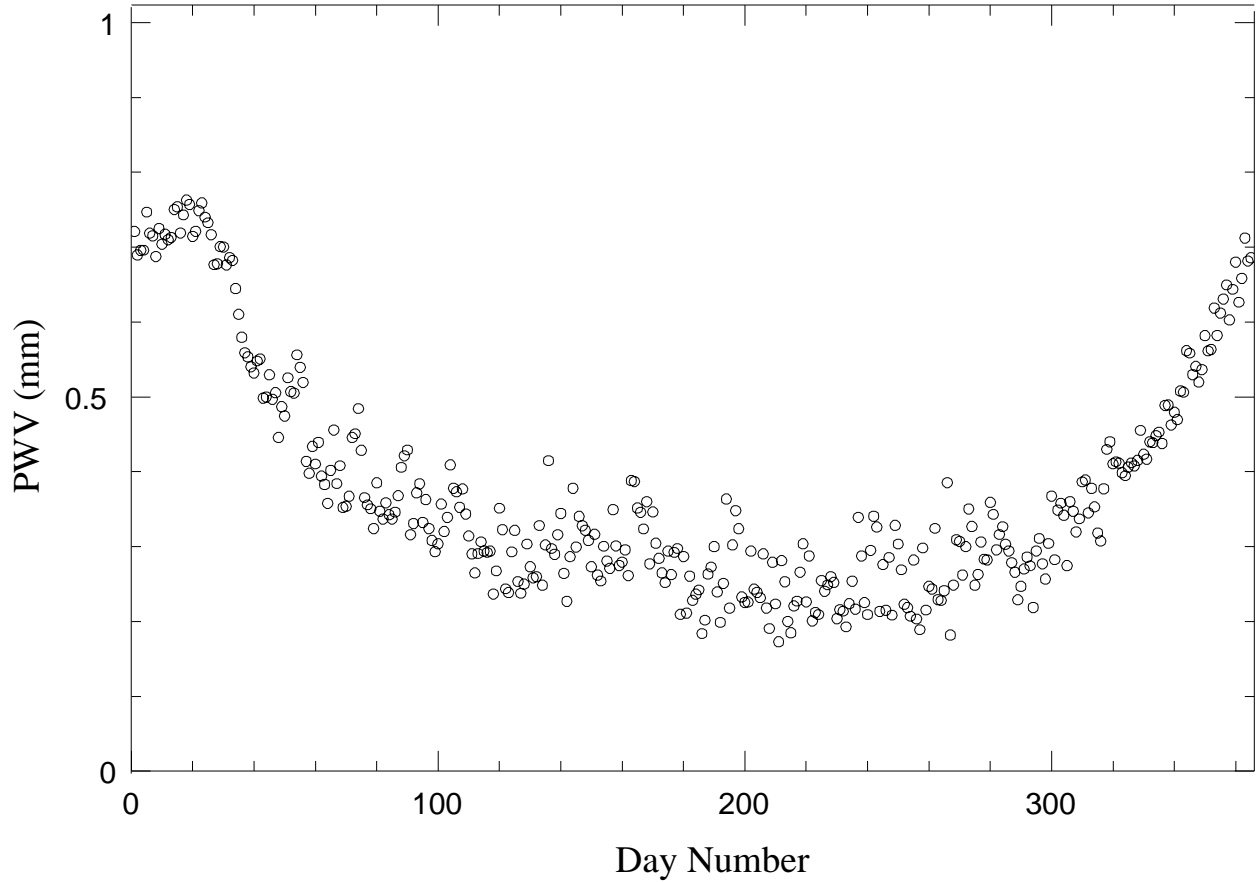


Fig. 4.— **Average PWV at Pole by day of year, 1961-1999, adapted from Chamberlin (2000).** The PWV in millimeters for each day of the year between 1961 and 1999 is averaged and plotted as a function of day of year. This plot shows the average seasonal trend, where the average water vapor content of the atmosphere declines from February through September.

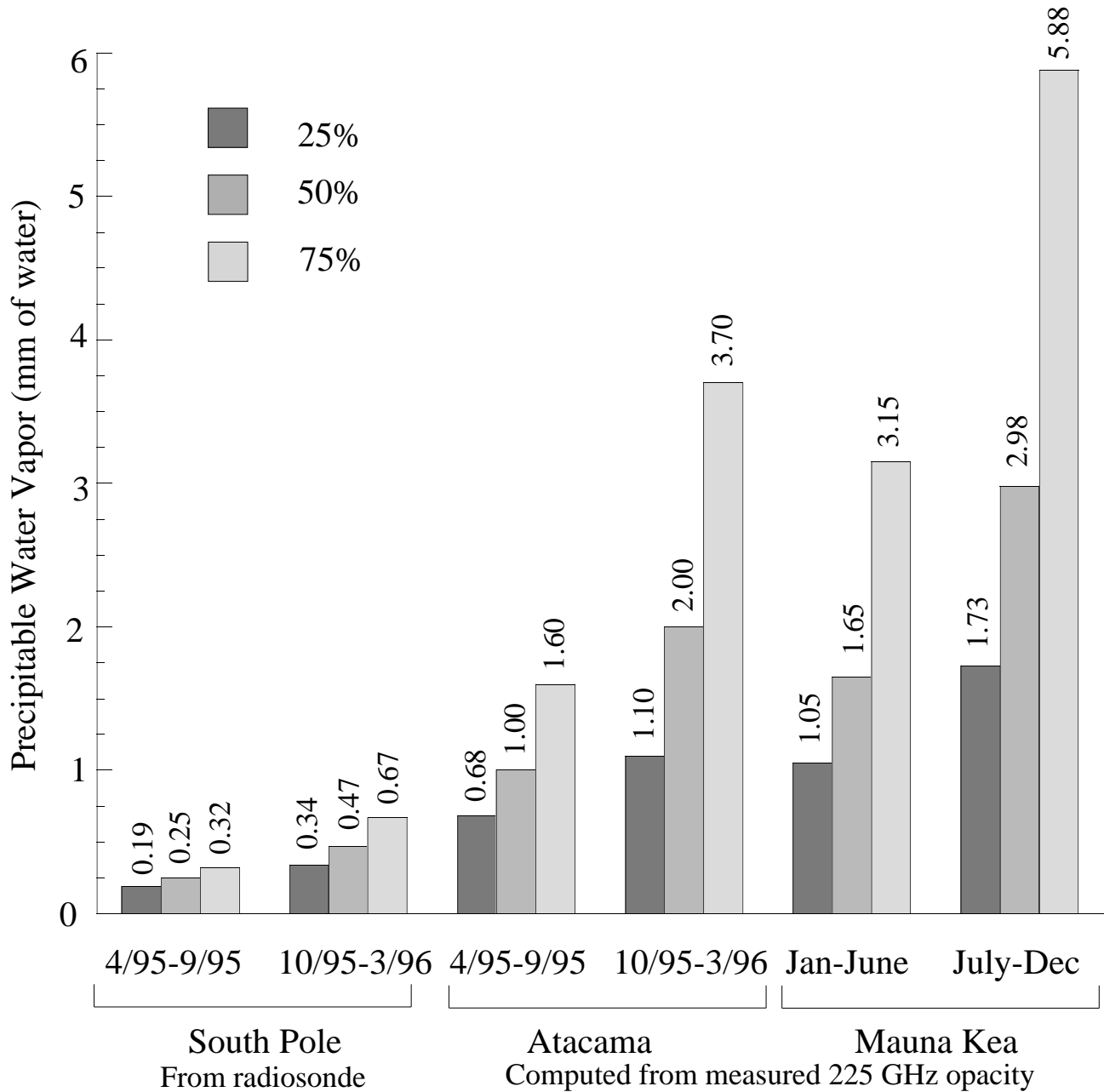


Fig. 5.— **Quartiles of Precipitable Water Vapor at Three Sites, from Lane (1998).** The South Pole is a considerably drier site than Mauna Kea or Atacama (Chajnantor). During the wettest quartile at the South Pole, the total precipitable water vapor is lower than during the driest quartile at either Mauna Kea or Atacama.

observations at 492 GHz (609  $\mu\text{m}$ ) with AST/RO during the 1995 observing season. Even though this frequency is near a strong oxygen line, the opacity was below 0.70 half of the time during the Austral winter and reached values as low as 0.34, better than ever measured at any ground-based site. The stability was also remarkably good: the opacity remained below 1.0 for weeks at a time. The 225 GHz (1.33 mm) skydip data for the Pole were obtained during 1992 (Chamberlin & Bally 1994, 1995) using a standard NRAO tipping radiometer similar to the ones used to measure the 225 GHz zenith opacities at Mauna Kea and Chajnantor, and the results are summarized by Chamberlin et al. (1997) and Lane (1998). The tight linear relation between 225 GHz skydip data and balloon sonde PWV measurements is discussed by Chamberlin & Bally (1995).

From early 1998, the 350 $\mu\text{m}$  (850 GHz) band has been continuously monitored at Mauna Kea, Chajnantor, and South Pole by identical tipper instruments developed by S. Radford of NRAO and J. Peterson of Carnegie-Mellon U. and CARA. Results from South Pole are compared to Chajnantor and Mauna Kea in Figure 6. These instruments measure a broad band that includes the center of the 350  $\mu\text{m}$  window as well as more opaque nearby wavelengths. Comparison of the  $\tau$  values measured by these instruments is tightly correlated with occasional narrow-band skydip measurements made within this band by the CSO and AST/RO; the narrow band  $\tau$  values are about a factor of two smaller than those output by the broadband instrument. *The 350 $\mu\text{m}$  opacity at the South Pole is consistently better than at Mauna Kea or Chajnantor.* If three identical background-limited instruments operating in the 350  $\mu\text{m}$  window were placed at Pole, Chajnantor, and Mauna Kea to do identical observations over a long period of time, the observations at Pole would proceed 110 $\times$  faster than Mauna Kea and 4.5 $\times$  faster than Chajnantor.

The success or failure of various submillimeter-wave observational techniques depend critically on atmospheric opacity. Just as it makes no sense to carry out visual-wavelength

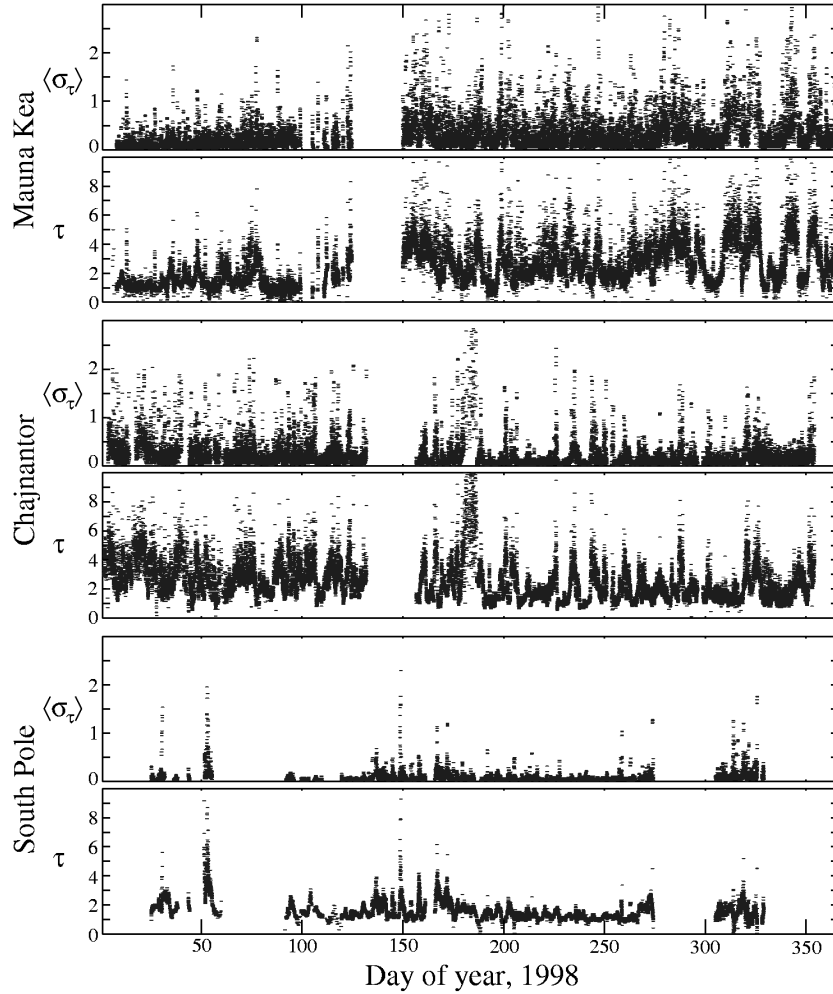


Fig. 6.— **Sky Noise and Opacity Measurements at 350  $\mu\text{m}$  from Three Sites.** These plots show data from identical NRAO-CMU 350  $\mu\text{m}$  broadband tippers located at Mauna Kea, the ALMA site at Chajnantor, and South Pole during 1998. The upper plot of each pair shows  $\langle\sigma_\tau\rangle$ , the rms deviation in the opacity  $\tau$  during a one-hour period—a measure of sky noise on large scales; the lower plot of each pair shows  $\tau$ , the broadband 350  $\mu\text{m}$  opacity. The first 100 days of 1998 on Mauna Kea were exceptionally good for that site. During the best weather at the Pole,  $\langle\sigma_\tau\rangle$  was dominated by detector noise rather than sky noise. Data courtesy of S. Radford and J. Peterson.



photometry in cloudy weather, there is an atmospheric opacity above which any particular submillimeter-wave observational technique will fail to give usable results. This threshold depends on the details of the particular technique and its sensitivity to the spectrum of atmospheric noise, but for many techniques the threshold lies near  $\tau \sim 1$ . Weather conditions above the threshold cannot be compared to those below the threshold by simple Gaussian noise analysis: ten days where  $\tau \approx 1.5$  can never be the equivalent of one day where  $\tau \approx 0.5$ . For deep background experiments, it is important to choose the best possible site.

*Sky noise* refers to fluctuations in total power or phase of a detector caused by variations in atmospheric emissivity and path length on timescales of order one second. Sky noise causes systematic errors in the measurement of astronomical sources. In an instrument that is well-designed, meaning that it has no intrinsic systematic errors, the sky noise will determine the minimum flux that can be observed, the flux below which the instrument will no longer “integrate down”. This flux limit is proportional to the power in the sky noise spectral energy distribution at the switching frequency of the observing equipment. Lay & Halverson (2000) show analytically how sky noise causes observational techniques to fail: fluctuations in a component of the data due to sky noise integrates down more slowly than  $t^{-1/2}$  and will come to dominate the error during long observations. Sky noise is a source of systematic noise which is not within the control of the instrument designer, and the limits to measurement imposed by sky noise are frequently reached in ground-based submillimeter-wave instrumentation.

Sky noise at the Pole is considerably smaller than at other sites at the same opacity. As discussed by Chamberlin & Bally (1995) and Chamberlin (2000), the PWV at the Pole is often so low that the opacity is dominated by the *dry air* component; the *dry air* emissivity and phase error do not vary as strongly or rapidly as the emissivity and phase error due to

water vapor. The spectral energy density of sky noise is determined by turbulence in the atmosphere and has a roughly similar spectral shape at all sites (Lay & Halverson 2000). Measurement of spectral noise at one frequency can therefore be extrapolated to other frequencies.

Figure 6 gives a direct indication of sky noise at submillimeter wavelengths at the largest timescales. The value  $\langle\sigma_\tau\rangle$  is the root-mean-square deviation of opacity measurements made within an hour’s time. As a measure of sky noise, this value has two defects: (1) during the best weather it is limited by detector noise within the NRAO-CMU tipper (which uses room-temperature bolometers) rather than sky noise and (2) the  $\sim 10^{-3}$  Hz fluctuations it measures are at much lower frequencies than the switching frequencies used for astronomical observations, so  $\langle\sigma_\tau\rangle$  is an upper limit to sky noise at very low frequencies. Figure 6 nevertheless gives a clear indication that the power in sky noise at Pole is often several times less than at Mauna Kea or Chajnantor.

Other instruments are sensitive to sky noise at frequencies near 10 Hz and can be used to give quantitative results over more limited periods of time. Sky noise at the Pole has been measured in conjunction with cosmic microwave background experiments at the Pole on Python (Alvarez 1995; Dragovan et al. 1994; Ruhl et al. 1995; Platt et al. 1997; Coble et al. 1999) and White Dish (Tucker et al. 1993). Python, with a 2.75 deg throw, had  $1 \text{ mK Hz}^{-1/2}$  sky noise on a median summer day, whereas White Dish, which had a 0.5 deg throw, was much less affected by sky noise. Extrapolating to 218 GHz and a 0.2 deg throw, the median sky noise is estimated to be  $150 \mu\text{K Hz}^{-1/2}$  even in the Austral summer, lower by a factor of ten than the sky noise observed during Sunyaev-Zel’dovich (S-Z) effect observations on Mauna Kea (Holzapfel et al. 1997).

Lay & Halverson (2000) have compared the Python experiment at Pole with the Site Testing Interferometer at Chajnantor (Radford et al. 1996; Holdaway et al. 1995). These

are very different instruments, but the differences can be bridged by fitting to a parametric model. Lay & Halverson (2000) have developed an atmospheric model for sky noise with a Kolmogorov power law with both three- and two-dimensional regimes, and have applied it to data from Python and the Chajnantor Testing Interferometer. They find that the amplitude of the sky noise at the Pole is 10 to 50 times less than that at Chajnantor. *Sky noise at the South Pole is significantly less than at other sites.*

### 3. Instrument and Capabilities

#### 3.1. Receivers

Currently, there are four heterodyne receivers mounted on an optical table suspended from the telescope structure in a spacious ( $5\text{m} \times 5\text{m} \times 3\text{m}$ ), warm Coudé room:

- a 230 GHz SIS receiver, 110–150 K single-sideband (SSB) noise temperature;
- a 450–495 GHz SIS waveguide receiver, 200–400 K DSB (Walker et al. 1992);
- a 450–495 GHz SIS quasi-optical receiver, 165–250 K DSB (Engargiola et al. 1994; Zmuidzinas & LeDuc 1992);
- a 800–820 GHz fixed-tuned SIS waveguide mixer receiver, 950–1500 K DSB (Honingh et al. 1997).

The currently available backends are: two acousto-optical spectrometers (AOS) with 1.07 MHz resolution, 1.1 GHz bandwidth, and 2048 channels each, and one high-resolution AOS with 44 kHz resolution, 64 MHz bandwidth, and 2048 channels (Schieder et al. 1989).

Table 1: Physical Environment of the AST/RO Telescope

Altitude	2847 m
Longitude	W 45°53'
Latitude	S 89°59'40"
Average Pressure <sup>a</sup>	680 mb
Minimum Temperature <sup>a</sup>	–82 C
Maximum Temperature <sup>a</sup>	–14 C
Average Temperature <sup>a</sup>	–49 C
Average 24-hour Temperature variation <sup>b</sup>	6.1 C
Average Wind Speed <sup>a</sup>	5.8 m s <sup>–1</sup>
Maximum Wind Speed <sup>a</sup>	24 m s <sup>–1</sup>
Annual Average Cloud Cover	
clear	31%
scattered	27%
Rainfall <sup>a</sup>	0
Median Water Vapor Column in summer <sup>c</sup>	0.47 mm PWV
Median Water Vapor Column in winter <sup>c</sup>	0.25 mm PWV
Best 5% Water Vapor Column in winter <sup>c</sup>	0.10 mm PWV
Median Observed Zenith Transmission at 609 $\mu$ m	
Wavelength in winter <sup>c</sup>	0.50
Median Calculated Zenith Transmission at 350 $\mu$ m	
Wavelength in winter <sup>d</sup>	0.76

---

<sup>a</sup>Schwerdtfeger 1984

<sup>b</sup>in 1992

<sup>c</sup>Lane 1998

<sup>d</sup>Bally 1989

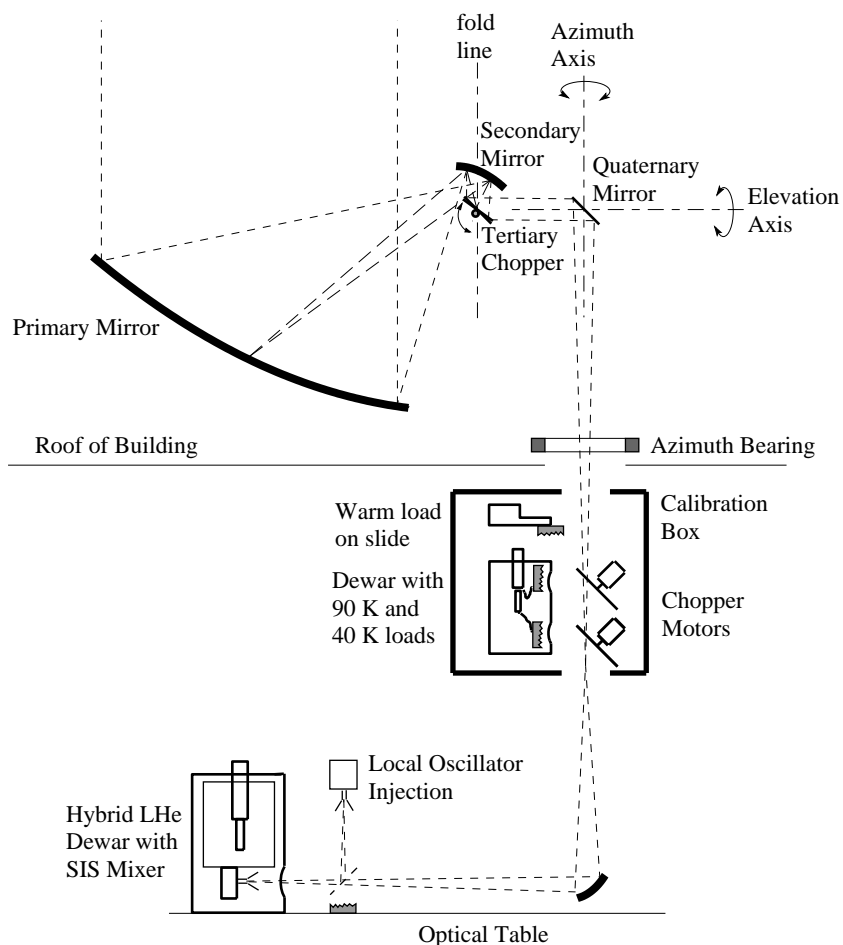


Fig. 7.— **Schematic of the AST/RO optical system.** For purposes of representation, the beam path has been flattened and the reader should imagine that the primary and secondary mirrors are rotated by  $90^\circ$  out of the plane of the page around the vertical “fold line”. Note that rays diverging from a point on the primary mirror reconverge at the chopping tertiary mirror, since the tertiary is at the exit pupil of the instrument. The tertiary and quaternary mirrors are flat. The calibration loads are in a dewar to the side of the Coudé beam entering along the azimuth axis. The ambient temperature load is on a linear actuator and can slide in front of the sky port. Motorized chopper mirrors switch the receiver beam from the cooled loads to the sky or to the ambient temperature load.

### 3.2. Optics

All of the optics in AST/RO are offset for high beam efficiency and avoidance of inadvertent reflections and resonances. Figure 7 shows the optical arrangement in its Coudé form. The primary reflector is made of carbon fiber and epoxy with a vacuum-sputtered aluminum surface having a surface roughness of  $6\mu\text{m}$  and an rms figure of about  $9\mu\text{m}$  (Stark 1995). The Gregorian secondary is a prolate spheroid with its offset angle chosen using the method of Dragone (1982), so that the Gregorian focus is equivalent to that of an on-axis telescope with the same diameter and focal length. The diffraction-limited field-of-view is  $2^\circ$  in diameter at  $\lambda 3\text{mm}$  and  $20'$  in diameter at  $\lambda 200\mu\text{m}$ . The chopper can make full use of this field-of-view, because it is located at the exit pupil and so does not change the illumination pattern on the primary while chopping. Figure 8 shows the beamsize and displacement as a function of chopper angle. Note in Figure 7 that rays diverging from a point on the primary mirror reconverge at the tertiary mirror, since the tertiary is at the exit pupil of the instrument. Optimizing the optics this way requires that the primary mirror be cantilevered away from the elevation axis: this is accomplished with a truss of Invar rods which hold the primary-to-secondary distance invariant with temperature. When the fourth mirror shown in Figure 7 is removed, the telescope has a Nasmyth focus where the beam passes through an elevation bearing which has a 0.2m diameter hole. Array detectors of various types can be used at this focus.

## 4. Observing Considerations

### 4.1. Focus

The secondary mirror is mounted on a computer-controlled positioning stage which allows the secondary mirror to be translated in three dimensions: a focus translation along

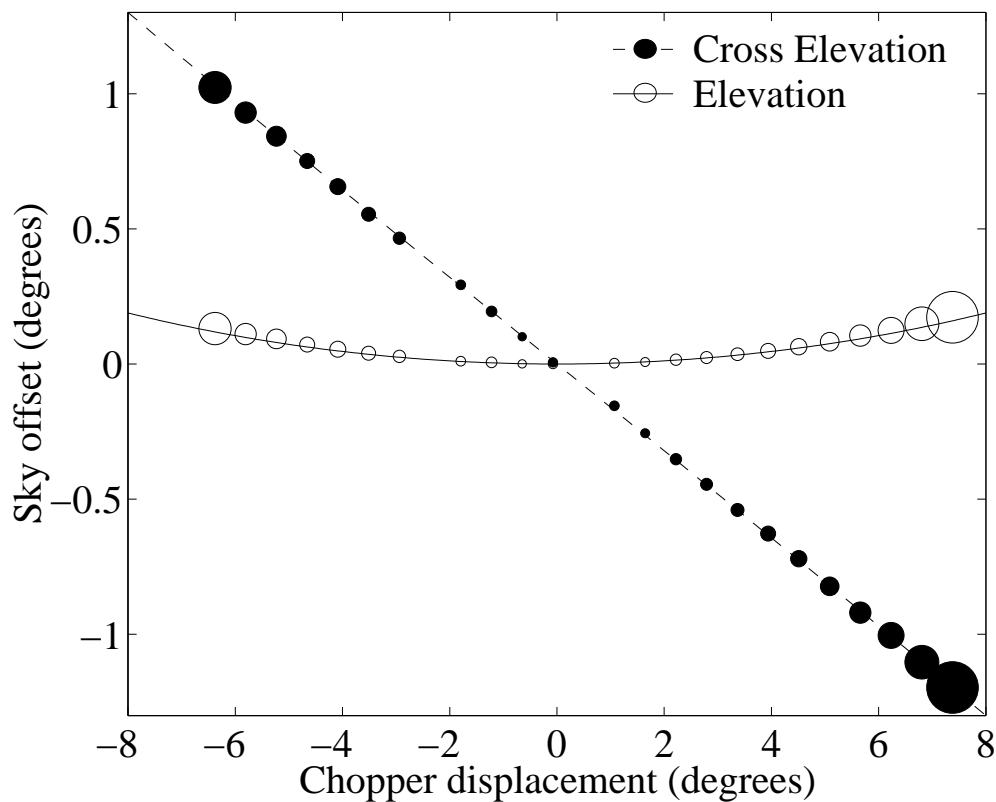


Fig. 8.— **Measurements of the AST/RO chopper.** Beam position is measured as a function of chopper displacement. Shown are elevation and cross-elevation pointing offsets as a function of chopper motion. The ellipses represent beam size and position data measured during scans of the moon at  $\lambda 600\mu\text{m}$ ; each ellipse is similar in shape to the beamshape at that chopper displacement, and the size of each ellipse is given by the scale on the ordinate axis. The curves are calculations of beam centroid based on a computer model of the optics.

the ray from the center of the primary to the center of the secondary, translation parallel to the elevation axis, and translation in a direction perpendicular to these two directions. The angular alignment of the secondary is not adjustable, but it does not need to be: as described in Stark et al. (1997), the primary mirror is aligned relative to the secondary mirror by mechanical means. This procedure sets the angular alignment. Figure 9 shows the horizontal and vertical beam size as a function of the focus adjustment, as measured by scans of the moon. The data compare well with theoretical expectation near the point of best focus where the beam has a nearly gaussian shape; the deviations between theory and measured points increase as the gaussian approximation fails away from the point of best focus.

## 4.2. Optical Pointing

Telescope pointing is controlled by the main data acquisition computer, shown schematically in Figure 10. Inputs to the computer are time from the Global Positioning Satellite receiver and encoder readouts from both antenna axes. Outputs from the computer are the commanded velocities of the antenna axis motors. The commanded velocity is calculated from the difference between the encoder readouts and a *command position*, which is in turn calculated from the time, the telescope position required by the observing program, and the *pointing model*. The telescope drive system, as described in Stark et al. (1997), is a mostly analog electronic servo mechanism capable of driving the telescope so that the encoder reading differs from the position commanded by the computer by less than one second of arc for antenna velocities near the sidereal rate. The pointing model characterizes the imperfections in the telescope construction, such as gravitational sag, bearing misalignments, and manufacturing errors.

The pointing model is determined by measurements of the positions of stars with a



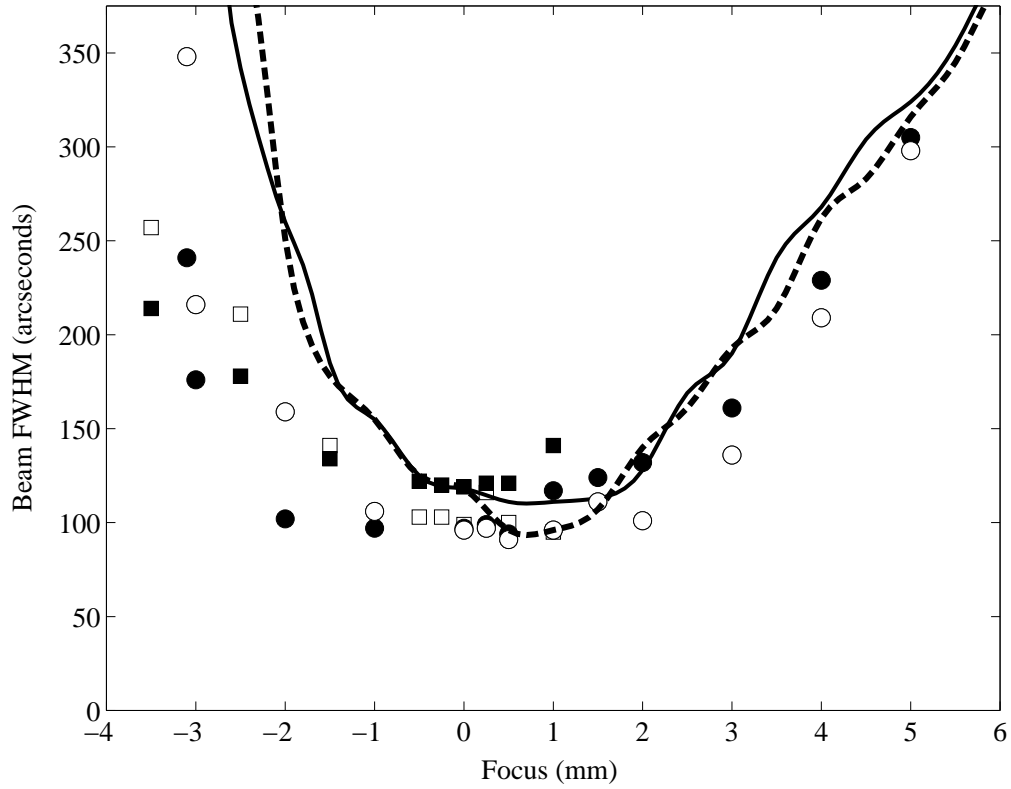


Fig. 9.— **Theoretical and measured focus curves for AST/RO.** The horizontal (filled symbols, solid line) and vertical (open symbols, dashed line) beam size plotted as a function of focus adjustment. Positive focus adjustment moves the primary and secondary mirrors closer together. Data plotted as circles were obtained using the 460 GHz waveguide receiver; data plotted as squares were obtained using the 492 GHz quasi-optical receiver. The solid and dashed lines represent results calculated from a model of the AST/RO optical system, assuming a 17.5 dB edge taper.

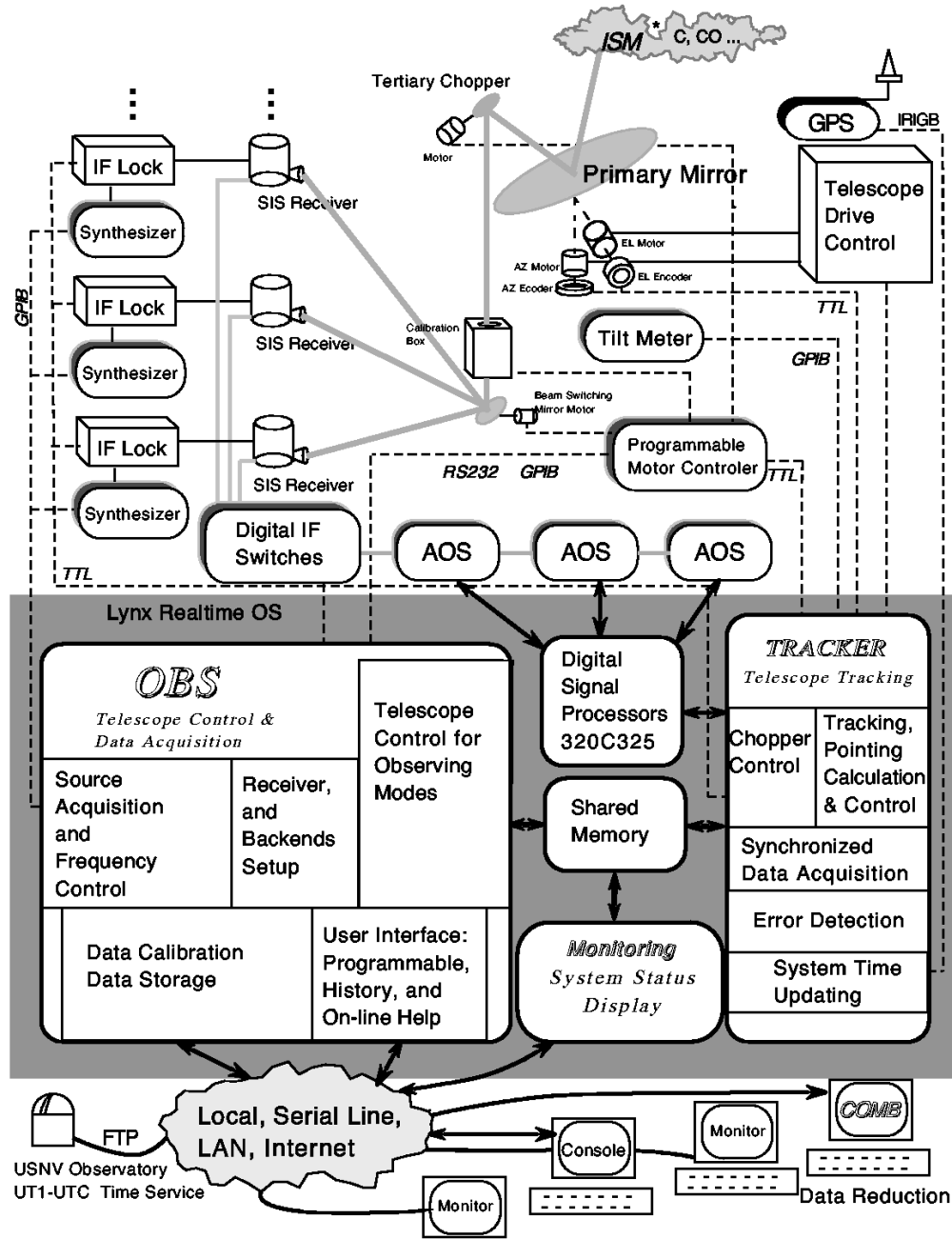


Fig. 10.— Schematic of the AST/RO control system. This block diagram shows the complexity of the AST/RO system. Using a variety of interfaces and protocols, the computer monitors and controls the hardware subsystems to carry out the processes that constitute a radioastronomical observation. The data acquisition computer is shown as a shaded area.

guide telescope mounted on AST/RO’s elevation structure. The guide telescope consists of a 76mm diameter, 750 mm focal length lens mounted at one end of a 100mm diameter carbon fiber-reinforced epoxy tube and an Electrim EDC-1000N CCD camera mounted at the other end on a focussing stage. The telescope tube is filled with dry nitrogen gas, sealed, warmed with electrical tape, and insulated. It works well under all South Pole conditions. In front of the lens is a deep red filter to facilitate detection of stars in daylight. Daylight observing capability is critical since the telescope is available to engineering and test teams only during the daylight summer months. The CCD camera is connected to a readout and control board in the data acquisition computer.

Following Condon (1992), the horizontal pointing error  $\Delta Az \cos(El)$  can be expressed as:

$$\begin{aligned} \Delta Az \cos(El) = & C_1 + C_2 \cos(El) + C_3 \sin(El) + C_4 \cos(El) \sin(El) \\ & + C_5 \sin(El) \sin(El) + C_6 \cos(2Az) \cos(El) + C_7 \sin(2Az) \cos(El) \\ & + C_8 \cos(3Az) \cos(El) + C_9 \sin(3Az) \cos(El) \quad , \end{aligned} \quad (1)$$

where  $C_1$  is the optical telescope horizontal collimation error,  $C_2$  is the constant azimuth offset (encoder zero point offset),  $C_3$  is the elevation axis horizontal offset,  $C_4$  and  $C_5$  represent the tilt from vertical of the azimuth axis, and  $C_6$  through  $C_9$  represent irregularities in the bearing race of the azimuth bearing. The vertical pointing error  $\Delta El$  can be expressed as:

$$\begin{aligned} \Delta El = & D_1 + D_2 \cos(El) + D_3 \sin(El) + D_4 \cos(Az) \\ & + D_5 \sin(Az) + D_6 \cos(2Az) + D_7 \sin(2Az) \\ & + D_8 \cos(3Az) + D_9 \sin(3Az) \quad , \end{aligned} \quad (2)$$

where  $D_1$  is the optical telescope vertical collimation error plus encoder offset,  $D_2$  and  $D_3$  are mechanical sag and elevation encoder decentering,  $D_4$  and  $D_5$  represent the tilt from

vertical of the azimuth axis, and  $D_6$  through  $D_9$  represent irregularities in the bearing race.

A pointing data set consists of position offsets  $(\Delta Az_i, \Delta El_i)$  as a function of  $(Az_i, El_i)$ , for several hundred observations of stars ( $i = 1, \dots, N$ ). The  $\Delta El_i$  values are corrected for optical refraction:  $\Delta El(\text{refraction}) = -51.84'' \cot(El)$ . The best fit values  $C_1, \dots, C_9$  and  $D_1, \dots, D_9$  in Equations 1 and 2 are solved for as a function of the observed star positions and offsets. This is an inverse linear problem solved by standard numerical methods. The  $C_1, \dots, C_9$  and  $D_1, \dots, D_9$  constants are then inserted into the real-time telescope drive system control software as corrections to the pointing. With this pointing model in place, subsequent observations of stars show errors of only a few seconds of arc. This pointing process is repeated yearly. The high-order terms,  $C_6, \dots, C_9$  and  $D_6, \dots, D_9$  have not changed significantly since they were first measured in 1993. The low-order terms,  $C_1, \dots, C_5$  and  $D_1, \dots, D_5$  change because of instabilities in the mechanical mounting of the guide telescope, long-term shifts in the telescope foundations, and thermal heating of the telescope tower when the sun is up.

### 4.3. Radio Pointing

Implementation of the optical pointing mechanism assures that the optical telescope boresight attached to the telescope’s elevation structure is pointed within specification. The radio receivers are, however, located at a Coudé focus, which is attached to the telescope mounting tower and fixed with respect to the earth. As shown in Figure 7, the tertiary and quaternary steer the radio beam along the elevation and azimuth axes. Since the alignment of these mirrors is not perfect, additional corrections are needed for pointing each receiver (Zhang 1996).

In Figure 11, the elevation axis intersects the tertiary at  $O_1$  and the quaternary at  $O_2$ .

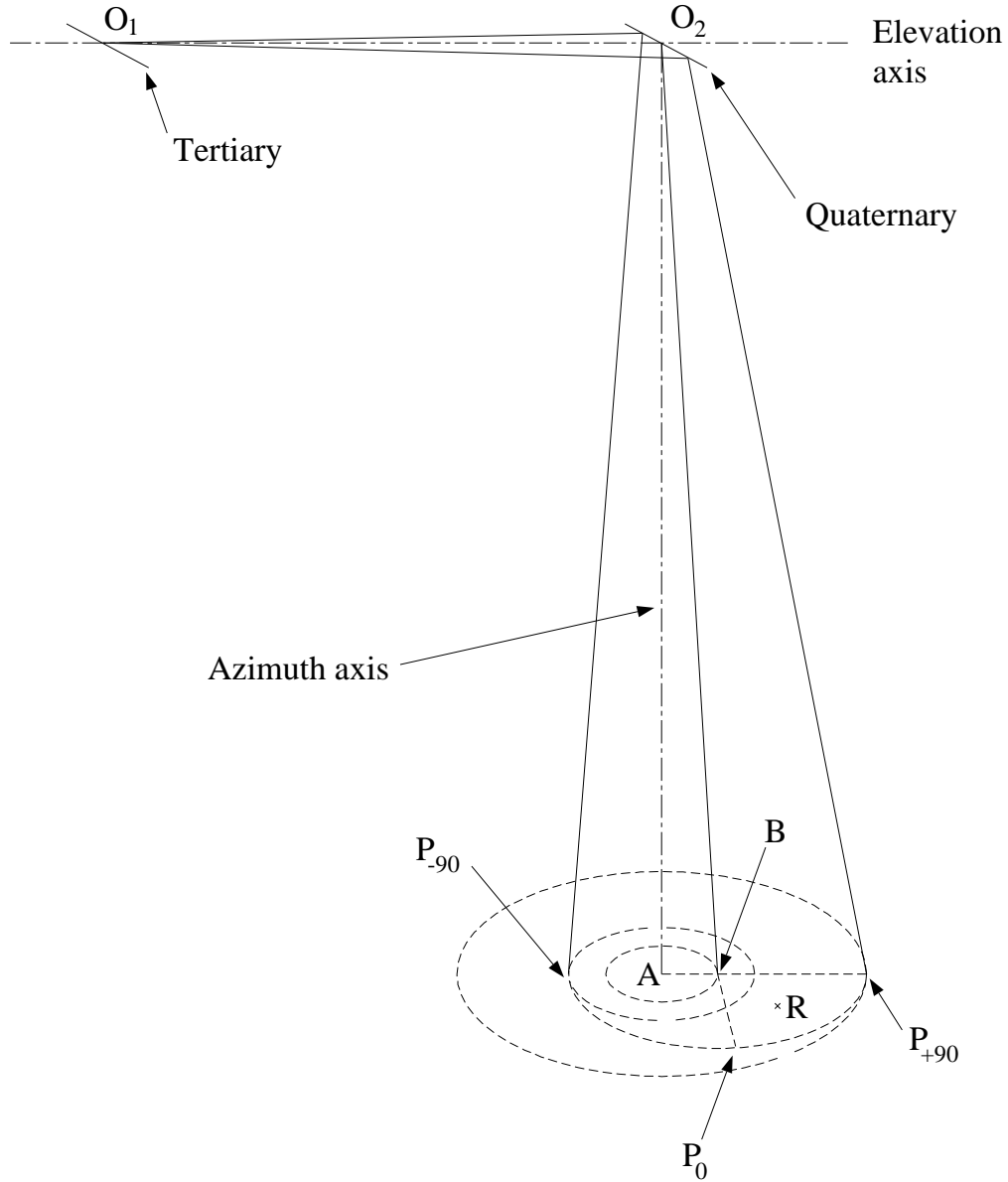


Fig. 11.— Geometry of AST/RO optics from the tertiary mirror to the Coudé focus (adapted from Zhang 1996). In general, the vectors  $\vec{AB}$  and  $B\vec{P}_{+90}$  are not parallel, nor do they lie in the same plane as the azimuth and elevation axes.

The intersection of the mechanical azimuth axis with the Coudé focal plane is point  $A$ . A photon traveling from  $O_1$  to  $O_2$  and then reflected from the quaternary will arrive at the focal plane at a point  $B$ . Point  $B$  and point  $A$  are not coincident because of misalignment of the quaternary mirror. If the tertiary is also misaligned, then the principal ray from the secondary will not coincide with the elevation axis. The principal ray reflects from the tertiary and quaternary, and intersects the focal plane at a point whose position depends on the elevation angle,  $P_{El}$ . Figure 11 shows that the locus of points  $P_{El}$  describes a circle centered on point  $B$ . The three labeled points,  $P_{-90}$ ,  $P_0$ , and  $P_{+90}$  show the intersection of the principal ray with the focal plane at elevation angles of  $-90$ ,  $0$ , and  $+90$ . (Assume here that the elevation travel includes negative angles; in actuality the mechanical stops on AST/RO do not permit negative elevation angles.) Furthermore, when the telescope rotates around the azimuth axis, the points  $P_{-90}$ ,  $P_0$ ,  $P_{+90}$ , and  $B$  precess around point  $A$  in a fixed pattern. We therefore see that a star on the boresight will have an offset from  $A$  given by

$$\vec{AP} = (\vec{AB} + B\vec{P}_0 e^{\pm iEl}) e^{-iAz}, \quad (3)$$

where the plus or minus sign in the elevation dependence is determined by the nature of the tertiary misalignment.

The receivers are not in general aligned with the azimuth axis, so let point  $R$  be the center of the receiver beamwaist at the Coudé focus. The image precession effect as viewed by the receiver is

$$\begin{aligned} \vec{RP} &= \vec{RA} + \vec{AP} = \vec{RA} + (\vec{AB} + B\vec{P}_0 e^{\pm iEl}) e^{-iAz}, \\ &= |\vec{RA}| e^{i\theta_a} + (|\vec{AB}| e^{i\theta_b} + |B\vec{P}_0| e^{i[\theta_c \pm El]}) e^{-iAz} \\ &= |\vec{RA}| (\cos\theta_a + i \sin\theta_a) + |\vec{AB}| \cos(\theta_b - Az) + i |\vec{AB}| \sin(\theta_b - Az) \\ &\quad + |B\vec{P}_0| \cos(\theta_c \pm El - Az) + i |B\vec{P}_0| \sin(\theta_c \pm El - Az), \end{aligned} \quad (4)$$

where  $\theta_a$ ,  $\theta_b$ , and  $\theta_c$  are the phase angles of vectors  $\vec{RA}$ ,  $\vec{AB}$ , and  $B\vec{P}_0$ , respectively. The Cartesian components,  $x$ ,  $y$ , of the focal plane image viewed by the receiver changes with

the azimuth and elevation of the source as

$$x_{\vec{RP}} = |\vec{RA}| \cos \theta_a + |\vec{AB}| \cos(\theta_b + Az) + |\vec{BP}_0| \cos(\theta_c \pm El - Az), \quad (5)$$

and

$$y_{\vec{RP}} = |\vec{RA}| \sin \theta_a + |\vec{AB}| \sin(\theta_b + Az) + |\vec{BP}_0| \sin(\theta_c \pm El - Az). \quad (6)$$

These coordinates represent the point within the image plane of the Coudé focus which is observed by the receiver.

The radio beam pointing corrections modify the pointing of the telescope so that the nominal boresight falls on a particular receiver at all azimuth and elevation. These corrections are an inversion of the effect described by Equations 5 and 6:

$$\Delta Az \cos(El) = A_1 \cos(\theta_1 \mp El + Az) + A_2 \cos(\theta_2 \mp El) + A_3 \cos(\theta_3), \quad (7)$$

and

$$\Delta El = A_1 \sin(\theta_1 \mp El + Az) + A_2 \sin(\theta_2 \mp El) + A_3 \sin(\theta_3), \quad (8)$$

where  $A_1 e^{i\theta_1}$  corrects the error due to the misalignment of the receiver,  $A_2 e^{i\theta_2}$  corrects the misalignment of the quaternary,  $A_3 e^{i\theta_3}$  corrects for the combined misalignment of the primary, secondary, and tertiary plus any collimation offsets between the optical guide telescope and the radio beam. In this formulation, there are six constants and the unknown sign of the elevation dependence to be determined by fits to radio pointing data. As a practical matter, it is easy with AST/RO to obtain accurate radio data for a few bright sources at all azimuths, but known sources suitable for radio pointing are only found at a few elevations. Equations 7 and 8 are therefore modified to absorb the elevation dependence into the fitting constants:

$$\Delta Az \cos(El) = B_1(El) \cos[\theta_1(El) + Az] + B_2(El), \quad (9)$$

and

$$\Delta El = B_3(El) \sin[\theta_2(El) + Az] + B_4(El). \quad (10)$$

For each elevation, a series of radio maps is used to determine the six parameters  $B_1$ ,  $B_2$ ,  $B_3$ ,  $B_4$ ,  $\theta_1$ , and  $\theta_2$ . If the mount errors have been correctly compensated by Equations 1 and 2, then  $B_1 = B_3$  and  $\theta_1 = \theta_2$ . When these parameters are measured at several elevations, their value at all elevations is estimated by linear or quadratic interpolation in  $El$ .

#### 4.4. Data Calibration

The real brightness temperature of an astronomical source depends only on the intrinsic radiation properties of the source, whereas the measured antenna temperature is influenced by the efficiency of telescope-to-source radiation coupling and the conditions in the Earth’s atmosphere through which the radiation must propagate. Calibration converts from spectrometer output counts in the data acquisition computer to the source effective radiation temperature, correcting for atmospheric losses. The intermediate frequency (IF) output of a mixer in one of the AST/RO receivers is comprised of down-converted signals from both the upper and lower sidebands. The amplified IF signal is detected by an acousto-optical spectrometer (AOS). The result is a spectrum of data with values proportional to the incident power spectrum. Discussed in this section is the conversion of these data values to the *radiation temperature* scale,  $T_R^*$ .

The *chopper wheel* method of calibration was originally described by Penzias & Burrus (1973) and elaborated upon by Ulich & Haas (1976) and Kutner & Ulich (1981). The theory of absolute calibration of millimeter-wavelength data has not changed in its fundamentals since those papers were written, but the introduction of automated calibration loads at temperatures other than ambient has led to improvements in technique and a conceptual shift in the understanding of calibration parameters.

- The ambient chopper-wheel calibration method determined the relative gain of each



spectrometer channel at the time of the chopper-wheel measurement, and later applied that gain to the switched astronomical data, assuming that it had not changed. Data quality is improved by measuring the relative gain during the acquisition of the astronomical data using the “ $(S - R)/R$ ” technique, where  $S$  refers to the “on-source” (or signal) measurement and  $R$  refers to an “off-source” (or reference) measurement. Calibration of such a spectrum requires, however, determination of the *atmosphere-corrected system temperature*,  $T_{\text{sys}}^*$ .

- The *receiver temperature*,  $T_{\text{rx}}$ , and *sky temperature*,  $T_{\text{sky}}$ , are distinct quantities measuring different sources of noise in the system. The former is a property of the instrument and under the control of the observer, while the latter is a property of the ever-changing sky. Using the ambient chopper-wheel method, these two noise power levels cannot be determined independently, because there is only a single calibration load of known temperature; this means, for example, that it is not possible to determine whether a loss of observing sensitivity is caused by a problem with the receiver or an increase in atmospheric opacity.

**Relation between  $T_A$  and  $T_B$**  The *antenna temperature* for an astronomical source is defined as its brightness temperature in the Rayleigh-Jeans limit. If a radio telescope observes a source of specific intensity  $I_\nu$ , the source brightness temperature  $T_B$  at frequency  $\nu$  is given by the Planck function,

$$I_\nu \stackrel{T_B}{=} \frac{2h\nu^3}{c^2} \frac{1}{\exp(h\nu/kT_B) - 1} . \quad (11)$$

The blackbody emitter at temperature  $T_B$  described by this equation is often fictitious—the usual circumstance for submillimeter observations of the interstellar medium is that the observed flux,  $I_\nu$ , results from thermal processes in emitters at temperatures higher than  $T_B$  that do not fill the telescope beam or are not optically thick. The antenna temperature

is given by the Rayleigh-Jeans limit to Equation 11,

$$I_\nu \stackrel{T_A}{\equiv} \frac{2k\nu^2 T_A}{c^2} . \quad (12)$$

The *effective radiation temperature* is

$$J_\nu(T) \equiv \frac{h\nu/k}{\exp(h\nu/kT) - 1} . \quad (13)$$

In the Rayleigh–Jeans limit, ( $h\nu/k \ll T$ ),  $J_\nu(T) = T$ ; this approximation applies to essentially all temperatures within the AST/RO system, since  $h \cdot 1 \text{ THz}/k = 4.8 \text{ K}$ , which is considerably lower than any physical temperature found in the AST/RO calibration system, telescope, or the atmosphere. It must be remembered, however, that the small flux levels of observed astronomical sources are expressed in the  $T_A$  scale, which is simply defined to be proportional to power:  $T_A = (c^2/2k\nu^2) I_\nu$ . This is a linear extrapolation to low power levels from the higher power levels of the calibration loads, where the calibration loads do satisfy the Rayleigh–Jeans approximation at these frequencies. Setting Equations 11 and 12 equal, we see that antenna temperature is the effective radiation temperature of the source brightness temperature,

$$T_A = J_\nu(T_B) , \quad (14)$$

but in general  $T_A$  is small so that  $T_B \gtrsim T_A$ .

**Calibration scans.** The AST/RO calibration system allows the receivers to “chop” between three blackbody loads and the sky (Stark et al. 1997). There is a load at ambient receiver room temperature (the “warm” load), and two loads cooled by a closed cycle refrigerator to 40 K (the “cold” load) and 90 K (the “cool” load). The surfaces of the refrigerated loads are warmed to temperatures higher than their average physical temperature by infrared radiation entering the dewar windows, so that their effective radiation temperatures are about 100 K and 140 K, respectively. The effective radiation

temperatures of the loads are measured about once a month by manually comparing the receiver response to each load with that of an absorber soaked in liquid nitrogen and to the warm load. The physical temperatures of all the loads are monitored by the computer, and we assume that if the physical temperature has not changed, the effective radiation temperature has not changed either.

During a calibration scan (performed via the OBS command `ca`), the data acquisition computer records data for each AOS channel corresponding to the receiver response to (1) no incoming IF signal (*zero* measurement),  $D_{\text{zero}j}$  (this is essentially the dark current of the CCD output stage of the AOS), (2) the “cold” calibration load,  $D_{\text{cold}j}$ , and (3) the “warm” calibration load,  $D_{\text{warm}j}$ . The AOS operates as a linear power detector, i.e. the spectrum of measured data values  $D_j$  is proportional to the incident power spectrum. For the  $j$ th AOS channel, we measure the *gain*:

$$\Gamma_j = \frac{D_{\text{warm}j} - D_{\text{cold}j}}{J_\nu(T_{\text{warm}}) - J_\nu(T_{\text{cold}})} \quad . \quad (15)$$

The gains spectrum gives us the proportionality between the antenna temperature scale ( $T_A$ ) and the arbitrary intensity counts ( $D$ ) read out from the AOS by the computer. The *calibration spectrum* measures the noise of the receiver, IF system, and AOS:

$$T_{\text{rx}j} = \frac{D_{\text{cold}j} - D_{\text{zero}j}}{\Gamma_j} - J_\nu(T_{\text{cold}}) \quad . \quad (16)$$

The *average receiver noise temperature*,  $\langle T_{\text{rx}} \rangle$ , is the average of the calibration spectrum,

$$\langle T_{\text{rx}} \rangle \equiv \frac{1}{N_c} \sum_{j=1}^{N_c} T_{\text{rx}j} \quad . \quad (17)$$

where the average is performed over a selectable subset of spectrometer channels.

**The single-slab model of the atmosphere.** In the *single-slab model*, the atmosphere is assumed to be a plane-parallel medium with mean temperature  $T_{\text{at}}$  and zenith opacity  $\tau$ .

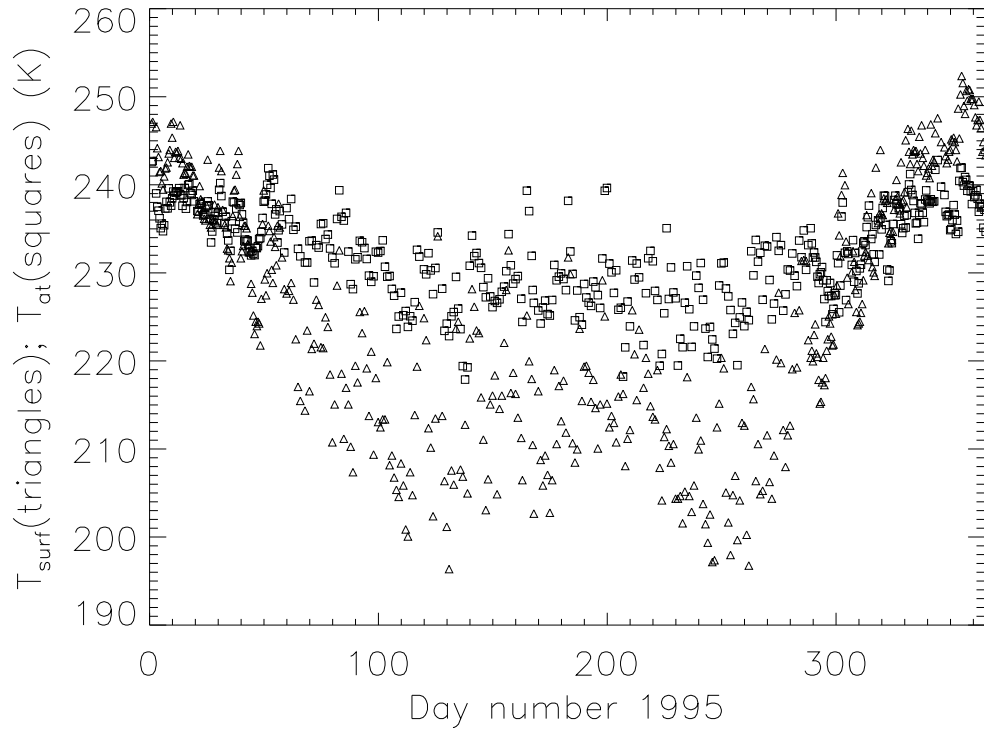


Fig. 12.—  $T_{at}$  and  $T_{surf}$  vs. time at the South Pole. Note the temperature inversion which occurs during the polar winter ( $T_{at} > T_{surf}$ ).

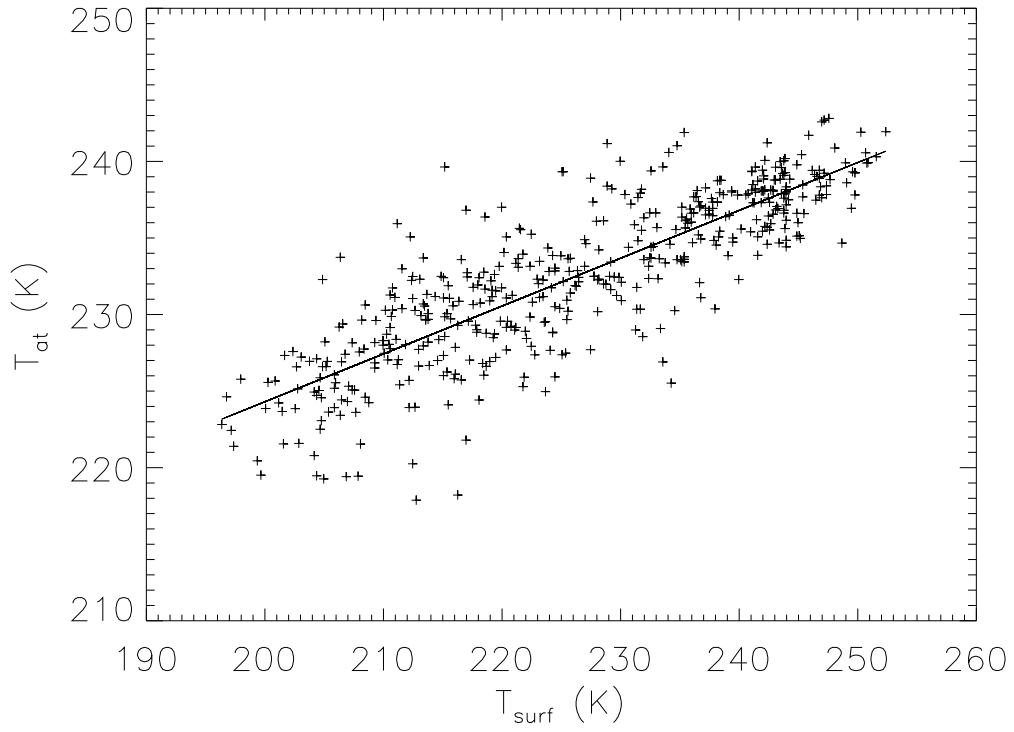


Fig. 13.—  $T_{\text{at}}$  vs.  $T_{\text{surf}}$  at the South Pole. The solid line shows the fit  $T_{\text{at}} = 0.31 T_{\text{surf}} + 162$  K.

The sky brightness temperature can be expressed as (Chamberlin et al. 1997)

$$T_{\text{sky}} = T_{\text{spill}} + \eta_l J_\nu(T_{\text{at}}) [1 - \exp(-\tau X)] \quad , \quad (18)$$

where we have introduced the *spillover temperature*,  $T_{\text{spill}}$ , the *telescope loss efficiency*,  $\eta_l$ , and  $X \equiv \csc(El)$  is the airmass at the elevation of the telescope. The effective radiation temperature of the cosmic microwave background radiation is ignored because it is negligible at submillimeter wavelengths. The telescope loss efficiency  $\eta_l$  is the fraction of receiver response that originates from the sky. The spillover temperature,  $T_{\text{spill}}$ , is the effective radiation temperature of all sources of radiation incident on the receiver which are not from the direction of the sky. These sources primarily include the thermal emission from the optics and spillover from the Earth’s surface.  $T_{\text{spill}}$  can be expressed as

$$T_{\text{spill}} = (1 - \eta_l) J_\nu(T_{\text{sbr}}) \quad , \quad (19)$$

where  $T_{\text{sbr}}$  is by definition the average temperature of the emitters giving rise to  $T_{\text{spill}}$  (Ulich & Haas 1976). Since there is a gradient in temperature between the air outside of the telescope and the warmed environment of the receiver room,  $T_{\text{sbr}}$  will fall somewhere between the outside surface temperature,  $T_{\text{surf}} \sim 230$  K, and the temperature of the receiver room,  $T_{\text{warm}} \approx 293$  K, depending on the quality of the receiver feed and its alignment.

**Sky brightness measurement.** The atmospheric attenuation of the signal is estimated by measuring the sky brightness temperature  $T_{\text{sky}}$ . The *sky spectrum* is made by measuring the sky and a cold load using the `sk` command in OBS. These are combined to yield:

$$T_{\text{sky}j} = \frac{D_{\text{sky}j} - D_{\text{cold}j}}{\Gamma_j} + J_\nu(T_{\text{cold}}) \quad , \quad (20)$$

and averaging over channels gives

$$\langle T_{\text{sky}} \rangle \equiv \frac{1}{N_c} \sum_{j=1}^{N_c} T_{\text{sky}j} \quad . \quad (21)$$

A *skydip* measures  $\langle T_{\text{sky}} \rangle$  for a range of different elevations. These data can be fit to the single-slab model (Equation 18) for the terms  $T_{\text{spill}}$  and  $\tau$ , and for the product  $\eta_l J_\nu(T_{\text{at}})$  (Chamberlin *et al.* 1997), which is used to determine  $\eta_l$ .

Instead of assuming that the mean atmospheric temperature,  $T_{\text{at}}$ , is equal to the ambient temperature,  $T_{\text{surf}}$ , which is standard chopper-wheel calibration procedure, we use actual *in situ* atmospheric measurements to deduce the mean atmospheric temperature. The South Pole meteorological station upper air balloon measures the air temperature and relative humidity as a function of height once or twice each day. These data can be used to derive  $T_{\text{at}}$ , the mean atmospheric temperature in the column of air above the telescope. For each balloon flight in 1995 and 1996, we have approximated  $T_{\text{at}}$  at  $\nu = 492$  GHz by averaging the physical temperature of the atmosphere,  $T$ , over altitude, weighted by the opacity of seven nearby water lines:

$$T_{\text{at}} \simeq \frac{\sum_{k=1}^7 \int_0^{z_{\text{max}}} T n_{\text{H}_2\text{O}} S_k(T) F_k(\nu_k, \nu) dz}{\sum_{k=1}^7 \int_0^{z_{\text{max}}} n_{\text{H}_2\text{O}} S_k(T) F_k(\nu_k, \nu) dz}, \quad (22)$$

where  $n_{\text{H}_2\text{O}}$  is the density of water vapor at height  $z$ ,  $\nu_k$  is the frequency of water line  $k$ ,  $S_k(T)$  is the line intensity of water line  $k$ , and  $F_k(\nu_k, \nu)$  is a Lorentzian line-broadening function. During the South Pole winter, a temperature inversion occurs where the mean atmospheric temperature,  $T_{\text{at}}$ , is higher than the surface temperature,  $T_{\text{surf}}$ . Figure 12 is a plot of  $T_{\text{at}}$  and  $T_{\text{surf}}$  vs. time for the year 1995. Despite the presence of this inversion layer for only part of the year,  $T_{\text{at}}$  is functionally related to  $T_{\text{surf}}$ , with little scatter. Figure 13 shows  $T_{\text{at}}$  vs.  $T_{\text{surf}}$  for 1995, with a straight line fit to the data. The fit to the 1996 data is the same. Adopting the relationship

$$T_{\text{at}} \approx 0.3 T_{\text{surf}} + 162 \text{ K} \quad (23)$$

represents ninety percent of the data within  $\pm 4$  K. Since  $T_{\text{at}} \approx 230$  K, this is a spread of only  $\pm 2\%$ . Given a value of the surface temperature when a skydip measurement was made,

this equation gives an estimate for  $T_{\text{at}}$ . The product  $\eta J_\nu(T_{\text{at}})$ , fit to skydip data, then gives an estimate of the telescope loss efficiency  $\eta$ . This procedure is most accurate during the best weather, when the fit to Equation 18 is best. We assume that for a given configuration of the optics and receivers,  $\eta$  is constant and independent of the weather. Values of  $\eta$  on AST/RO have ranged from 0.65 to 0.92 for various alignments of the various receivers.

In the AST/RO calibration system, the sky spectrum measurements are made several times each hour and are used to estimate the atmospheric opacity. Equations 18 and 19 can be rearranged to give:

$$\frac{e^{\tau X}}{\eta} = \frac{J_\nu(T_{\text{at}})}{\eta J_\nu(T_{\text{at}}) + (1 - \eta) J_\nu(T_{\text{sbr}}) - \langle T_{\text{sky}} \rangle}, \quad (24)$$

which is the multiplier needed to correct the data for atmospheric absorption and telescope loss efficiency (see Equation 42). Since  $T_{\text{at}} \approx T_{\text{sbr}} \approx T_{\text{surf}}$ , the denominator of this expression is essentially  $T_{\text{surf}} - \langle T_{\text{sky}} \rangle$ , with corrections. The entire expression depends only weakly on  $\eta$ .

**Single and Double Sideband Atmospheric Opacity.** For receiver systems with no method of sideband rejection, a given measurement is necessarily a *double-sideband* measurement. In other words, the measured response of an AOS channel is a combination of *two different frequencies*, the *signal* sideband and the *image* sideband, possibly with different gain in the two sidebands. The gains in the two sidebands are normalized so that  $g_s + g_i = 1$ .

A double-sideband measurement of the sky brightness temperature is weighted by the gain, as well as the atmospheric opacity, in each sideband,

$$T_{\text{sky}} = g_s T_{\text{spill}s} + g_i T_{\text{spill}i} + \eta J_\nu(T_{\text{at}}) [g_s(1 - e^{-\tau_s X}) + g_i(1 - e^{-\tau_i X})] \quad , \quad (25)$$

where  $\tau_s$  and  $\tau_i$  are the zenith opacities in the signal and image sidebands, respectively, and  $T_{\text{spill}s}$  and  $T_{\text{spill}i}$  are the spillover radiation temperatures at the frequencies  $\nu_s$  and  $\nu_i$ ,



respectively. Comparing Equations (25) and (18), we see that we can use the skydip fitting method if

$$T_{\text{spill}} \equiv g_s T_{\text{spill}s} + g_i T_{\text{spill}i} \quad (26)$$

and

$$e^{-\tau_{\text{dsb}}X} \equiv g_s e^{-\tau_s X} + g_i e^{-\tau_i X} \quad , \quad (27)$$

where the *double-sideband opacity* is  $\tau_{\text{dsb}}$  .

In order to calibrate a double-sideband measurement of an astronomical source, we relate the double-sideband opacity  $\tau_{\text{dsb}}$  to the opacity at the frequency of interest,  $\tau_s$ . As discussed by Chamberlin & Bally (1995), Chamberlin et al. (1997), and Chamberlin (2000), there is a linear relation between  $\tau_{\text{dsb}}$  and the amount of precipitable water vapor *PWV* above the South Pole:

$$\tau_{\text{dsb}} = A_{\text{dsb}} + B \cdot PWV \quad . \quad (28)$$

We will focus on the implications for double-sideband observations at 492.1607 GHz, the frequency of the  $^3P_1 \rightarrow ^3P_0$  transition of neutral atomic carbon [C I]. The opacity due to water vapor is a relatively broadband phenomenon. In the 492 GHz band, the slope  $B$  of Equation 28 does not vary rapidly with frequency. Chamberlin et al. (1997) find that  $B \approx 1.47$  at both 490.66 GHz and 493.66 GHz. The dry-air opacity  $A$ , however, varies strongly near 492 GHz, since this frequency is located on the wing of an O<sub>2</sub> line centered at 487.25 GHz.

Assume that the opacity in each sideband is a simple sum of the dry air opacity and the water vapor opacity

$$\tau_s = A_s + B \cdot PWV \quad ; \quad (29)$$

$$\tau_i = A_i + B \cdot PWV \quad .$$

Also assume that the value of  $B$  is constant over the frequency band of interest, and that the values of  $A_{\text{dsb}}$ ,  $A_s$ , and  $A_i$  are constant with time, *i.e.* the variation of  $\tau$  with time is strictly due to changes in PWV, and not, for example, to changes in barometric pressure. Substituting Equations 28 and 29 into Equation 27, and dividing by  $\exp(-B \cdot PWV)$ , we obtain

$$e^{-A_{\text{dsb}}X} = g_s e^{-A_s X} + g_i e^{-A_i X} . \quad (30)$$

Then, substituting the second of Equations 29 into Equation 27, we obtain

$$e^{-\tau_{\text{dsb}}X} = g_s e^{-\tau_s X} + g_i e^{-(A_i + B \cdot PWV)X} . \quad (31)$$

Since  $\tau_{\text{dsb}} = A_{\text{dsb}} + B \cdot PWV$ , this implies

$$\tau_s = \tau_{\text{dsb}} + (A_s - A_{\text{dsb}}) . \quad (32)$$

In practice,  $A_s$  is derived from a model of the atmosphere, and  $A_{\text{dsb}}$  and  $\tau_{\text{dsb}}$  are measured empirically. The measured values for  $A_{\text{dsb}}$  and  $\tau_{\text{dsb}}$  can be related to the predicted value for  $A_s$  by using the Atmospheric Transmission (AT) model of Grossman (1989), as modified by K. C. Yu and J. Bally for conditions at South Pole. The South Pole PWV levels applicable 10%, 25%, 50%, and 75% of the time during winter have been used to compute values of atmospheric transmittance as a function of wavelength (Fig. 14). For comparison, the transmittance for excellent conditions at Chajnantor is shown by the lowest dashed line in the figure.

The estimate made by Chamberlin *et al.* (1997) of  $A$ , which is based on double-sideband data, is necessarily a combination of  $A_i$  and  $A_s$  via Equation 30. The intermediate frequency used by AST/RO is 1.5 GHz. When the [C I] transition is in the lower sideband (LSB) and the local oscillator (LO) is tuned to 493.6607 GHz, the image sideband is at 495.1607 GHz. When the [C I] transition is in the upper sideband (USB), the local oscillator (LO) is tuned

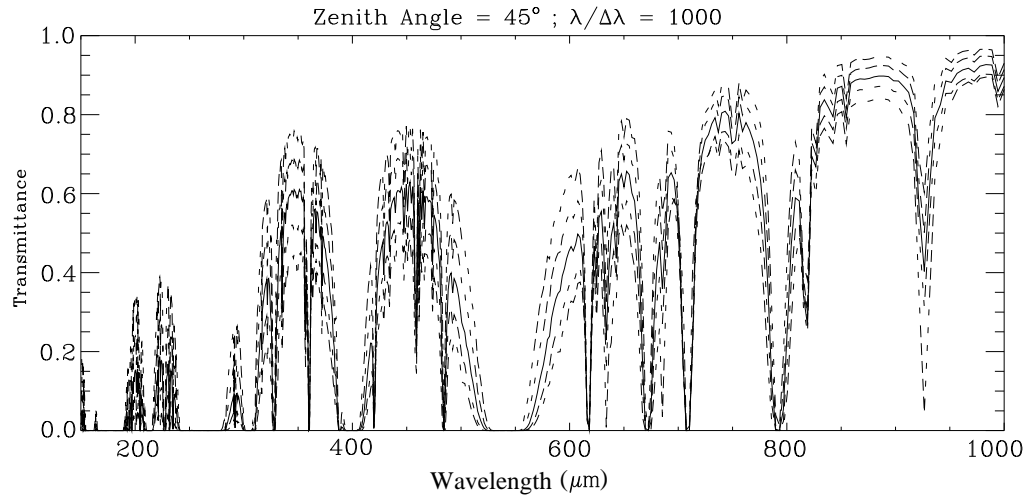


Fig. 14.— **Calculated Atmospheric Transmittance at South Pole, from Lane (1998).** Atmospheric transmittance at 1.41 airmasses calculated by K. C. Yu using Grossman’s AT code for the pressure, temperature, and water vapor content of the South Pole and Chajnantor. Values near  $609\mu\text{m}$  are consistent with AST/RO site testing. The upper four lines are for values of precipitable water vapor which are applicable 10%, 25%, 50%, and 75% of the time during winter (0.14 mm, 0.19 mm, 0.25 mm, and 0.32 mm, respectively). Also plotted (bottom dashed line) are values for the best 25% of the time during the better half of the year at Chajnantor (PWV = 0.68 mm). Note that at long wavelengths, the Chajnantor curve converges with the Pole curves. An explanation of the calculation and additional plots at other wavelengths and for other sites can be found at <http://casa.colorado.edu/~bally/AT/cara.html>.

to 490.6607 GHz, and the image sideband is at 489.1607 GHz, not far from the 487.25 GHz O<sub>2</sub> line.

Evaluating Equation 30 at the zenith ( $X = 1$ ) and multiplying by  $e^{A_s}$ , we obtain

$$e^{A_s} - A_{\text{dsb}} = g_s + g_i \frac{e^{-A_i}}{e^{-A_s}} \quad . \quad (33)$$

For the 492 GHz quasioptical receiver used to measure  $A_{\text{dsb}}$ , the gains in the two sidebands are equal,  $g_s = g_i = 1/2$ . Normalizing the data to the model predictions for the LSB frequency range, since it is furthest from the center of the O<sub>2</sub> line, and assuming that the dry air atmospheric *transmission* ratio  $e^{-A_i}/e^{-A_s}$  is as predicted by the AT model:  $e^{-A_i}/e^{-A_s} \approx 0.96/0.91 = 1.05$ . By Equation 33,  $(A_s - A_{\text{dsb}}^{\text{LSB}}) = 0.03$ , and, by Equation 32, we have the relationship between the LSB zenith opacity and the opacity at the signal frequency,

$$\tau_s \approx \tau_{\text{dsb}}^{\text{LSB}} \quad . \quad (34)$$

In other words, the double-sideband opacity derived from skydips made in LSB mode is a close approximation to the actual opacity at  $\nu_s = 492.1607$  GHz. Experimentally, Chamberlin *et al.* (1997) measure  $A_{\text{dsb}}^{\text{LSB}} = 0.33$ . Therefore, since  $(A_s - A_{\text{dsb}}^{\text{LSB}}) = 0.03$ , we have  $A_s \approx 0.36$ .

For the USB tuning, Chamberlin *et al.* (1997) measure  $A_{\text{dsb}}^{\text{USB}} = 0.57$ . Thus, by Equation 32,

$$\tau_s = \tau_{\text{dsb}}^{\text{USB}} - 0.21 \quad . \quad (35)$$

Thus the double-sideband opacity derived from USB skydips and  $T_{\text{sky}}$  measurements is greater than the actual opacity at  $\nu_s = 492.1607$  GHz by this constant offset.

**Double-Sideband Spectral Line Measurements.** The spectral line appears in only one of the sidebands. The source antenna temperature is a sum of contributions along the

line of sight from both the source and the sky. Following Ulich & Haas (1976),

$$T_{\text{source}j} = g_s [T_{\text{spill}S} + \eta_l J_\nu(T_{\text{at}})(1 - e^{-\tau_s X}) + \eta_l T_{A_j}^* e^{-\tau_s X}] \quad (36)$$

$$+ g_i [T_{\text{spill}i} + \eta_l J_\nu(T_{\text{at}})(1 - e^{-\tau_i X})] \quad ,$$

where  $T_{A_j}^*$  is the corrected antenna temperature of spectrometer channel  $j$ . Again, the cosmic microwave background radiation is ignored.

Observing always involves a switching scheme, where the frequency or position is changed and the signal on blank sky is subtracted from the signal on the source plus blank sky. In other words, subtracting Equation 25 from Equation 36 gives:

$$T_{A_j} \equiv T_{\text{source}j} - T_{\text{sky}j}$$

$$= g_s \eta_l T_{A_j}^* e^{-\tau_s X} \quad (37)$$

and shows the relation between corrected and uncorrected antenna temperature.

**Spectral Line Data Acquisition.** When observing the source, the average output of the  $j^{\text{th}}$  channel of the spectrometer is

$$D_{\text{source}j} = \Gamma_j (T_{\text{source}j} + T_{\text{rx}j}) + D_{\text{zero}j} \quad , \quad (38)$$

and when observing the reference, it is

$$D_{\text{ref}j} = D_{\text{sky}j} = \Gamma_j (T_{\text{sky}j} + T_{\text{rx}j}) + D_{\text{zero}j} \quad . \quad (39)$$

These quantities can be combined to yield a measurement of the antenna temperature of the source:

$$T_{A_j} = \frac{D_{\text{source}j} - D_{\text{ref}j}}{D_{\text{ref}j} - D_{\text{zero}j}} (T_{\text{sky}j} + T_{\text{rx}j}) \quad , \quad (40)$$

where  $T_{\text{sky}j}$  has been determined by the previous sky measurement (**sk**, Equation 20), and  $T_{\text{rx}j}$  and  $D_{\text{zero}j}$  have been determined by the previous calibration measurement (**ca**, Equation 16).

A better quality spectrum can be obtained by replacing  $T_{\text{sky}j}$  and  $T_{\text{rx}j}$  in Equation 40 by their average quantities  $\langle T_{\text{sky}} \rangle$  and  $\langle T_{\text{rx}} \rangle$ , from Equations 17 and 21:

$$T_{Aj} \cong \frac{D_{\text{source}j} - D_{\text{ref}j}}{D_{\text{ref}j} - D_{\text{zero}j}} (\langle T_{\text{sky}} \rangle + \langle T_{\text{rx}} \rangle) \quad . \quad (41)$$

This is because the actual noise power in the sky and from the receiver vary slowly across the bandpass of the spectrometer, whereas the calibration and sky spectra  $T_{\text{rx}j}$  and  $T_{\text{sky}j}$  show spurious variations caused by reflections from the surfaces of the calibration loads and the windows of the calibration dewar. For each spectrum, we define the *atmosphere-corrected system temperature*:

$$T_{\text{sys}}^* \equiv \frac{e^{\tau_s X}}{g_s \eta_l} (\langle T_{\text{sky}} \rangle + \langle T_{\text{rx}} \rangle) \quad , \quad (42)$$

where  $\langle T_{\text{rx}} \rangle$  has been determined by the most recent calibration,  $e^{\tau_s X}/\eta_l$  and  $\langle T_{\text{sky}} \rangle$  have been determined by the most recent sky brightness measurement at or near the elevation of the source (see Equation 24), and  $g_s$  has been determined by laboratory measurements of the receiver. We then see from Equations 41 and 37 that

$$T_{Aj}^* = \frac{D_{\text{source}j} - D_{\text{ref}j}}{D_{\text{ref}j} - D_{\text{zero}j}} T_{\text{sys}}^* \quad (43)$$

is the calibrated spectrum of the source. This is the “ $(S - R)/R$ ” method of data acquisition. It provides a high-quality spectrum of the source, because the gain of each channel,  $T_{\text{sys}}^*/(D_{\text{ref}j} - D_{\text{zero}j})$ , is measured during the course of the observation.

In the AST/RO system, the data acquisition program OBS writes the values  $T_{Aj}$  (usually calculated according to Equation 41— this is an option selectable by the observer) as *scan* data, and writes  $\eta_l$ ,  $g_s$ ,  $El$ ,  $\langle T_{\text{sky}} \rangle$ ,  $\langle T_{\text{rx}} \rangle$ ,  $T_{\text{surf}}$  together with about fifty other status variables, in the *scan header*. These data are converted to  $T_{Aj}^*$  by the command `gt` in the data reduction program COMB.

The *forward spillover and scattering efficiency*,  $\eta_{\text{fss}}$ , is defined by Kutner & Ulich (1981) to be the fraction of the telescope’s forward response which is also within the

diffraction pattern in and around the main beam. This quantity relates  $T_A^*$  to the *radiation temperature* of the source  $T_R^*$ , which is the recommended temperature scale for reporting millimeter-wave data (Kutner & Ulich 1981):  $T_R^* = T_A^*/\eta_{\text{fss}}$ . The unusual optics of the AST/RO telescope (Figure 7) give it feed properties similar to that of prime-focus designs, for which  $\eta_{\text{fss}} \approx 1.0$  (Kutner & Ulich 1981). When the AST/RO beam is pointed  $4'$  from the sun's limb, the excess  $T_A^*$  from the sun is less than 1% of the brightness of the sun's disk. This indicates  $1.0 \geq \eta_{\text{fss}} > 0.97$ , and so for AST/RO,  $T_R^* \approx T_A^*$ .

## 5. Conclusion

AST/RO is the first submillimeter-wave telescope to operate in winter on the Antarctic Plateau. During the first five years of observing, the most serious operational difficulties have been incapacitation of the single winterover scientist and lack of liquid helium; these problems are being addressed through allocation of additional resources and redundancy. Site testing and observation have demonstrated that the South Pole is an excellent site having good transparency and unusually low sky noise. This observatory is now a resource available to all astronomers on a proposal basis.

Rodney Marks died while serving as the year 2000 AST/RO winter-over scientist, and it is to him that this paper is dedicated. We thank Edgar Castro, Jeff Capara, Peter Cheimets, Jingquan Cheng, Robert Doherty, Urs Graf, James Howard, Gopal Narayanan, Maureen Savage, Rudolf Schieder, Oliver Siebertz, and Volker Tolls for their contributions to the project. Jonas Zmuidzinas generously provided examples of his excellent SIS mixer. We also thank Rick LeDuc and Bruce Bumble at JPL for making SIS junctions and Tom Phillips at Caltech for making them available to us. We thank Eric Silverberg and the Smithsonian Submillimeter Array Project for the optical guide telescope. We thank Simon

Radford of NRAO and Jeff Peterson of CMU for the data shown in Figure 6. The AST/RO group is grateful for the logistical support of the National Science Foundation (NSF), Antarctic Support Associates, Raytheon Polar Services Company, and CARA during our polar expeditions. This work was supported in part by National Science Foundation grant DPP88-18384, and by the Center for Astrophysical Research in Antarctica and the NSF under Cooperative Agreement OPP89-20223.



## REFERENCES

- Alvarez, D. L. 1995, PhD thesis, Princeton University
- Bally, J. 1989, in *Astrophysics in Antarctica*, ed. D. J. Mullan, M. A. Pomerantz, & T. Stanev (New York: American Institute of Physics), 100
- Chamberlin, R. A. 2000, *J. Geophys. Res.*, submitted
- Chamberlin, R. A., & Bally, J. 1994, *Appl. Opt.*, 33, 1095
- . 1995, *Int. J. Infrared and Millimeter Waves*, 16, 907
- Chamberlin, R. A., Lane, A. P., & Stark, A. A. 1997, *ApJ*, 476, 428
- Coble, K., et al. 1999, *ApJ*, 519, L5
- Condon, J. J. 1992, *GBT Pointing Equations*, GBT Technical Memorandum 75, NRAO
- Dragone, C. 1982, *IEEE Trans. Antennas and Propagation*, AP-30, 331
- Dragovan, M., Ruhl, J., Novak, G., Platt, S. R., Crone, B., Pernic, R., & Peterson, J. 1994, *ApJ*, 427, L67
- Engargiola, G., Zmuidzinas, J., & Lo, K.-Y. 1994, *Rev. Sci. Instr.*, 65, 1833
- Giovanelli, R., Darling, J., Sarazin, M., Eikenberry, S., Hoffman, W., Swain, M., Yu, J., Harvey, P., Otarola, A., & Valladares, G. 1999, *BAAS*, 30, 1264
- Hogg, D. 1992, *A Summary of the Data Obtained During the MMA Site Survey*, Millimeter Array Memo 79, NRAO
- Holdaway, M. A., Radford, S. J. E., Owen, F. N., & Foster, S. M. 1995, *Fast Switching Phase Calibration: Effectiveness at Mauna Kea and Chajnantor*, Millimeter Array Technical Memo 139, NRAO

- Holzappel, W. L., Arnaud, M., Ade, P. A. R., Church, S. E., Fischer, M. L., Mauskopf, P. D., Rephaeli, Y., Wilbanks, T. M., & E., L. A. 1997, *ApJ*, 480, 449
- Honingh, C. E., Hass, S., Hottgenroth, K., Jacobs, J., & Stutzki, J. 1997, *IEEE Trans. Appl. Superconductivity*, 7, 2582
- Kutner, M. L., & Ulich, B. L. 1981, *ApJ*, 250, 341
- Lane, A. P. 1998, in *Astrophysics from Antarctica*, ed. G. Novak & R. H. Landsberg, ASP Conf. Ser. 141 (San Francisco: ASP)
- Lane, A. P., & Stark, A. A. 1996, *Antarctic Journal of the U. S.*, 30, 377
- Lay, O. P., & Halverson, N. W. 2000, *ApJ*, in press, ([astro-ph/9905369](#))
- Masson, C. 1994, in *Astronomy with Millimeter and Submillimeter Wave Interferometry*, ed. M. Ishiguru & W. J. Welch, ASP Conf. Ser. 59 (San Francisco: ASP)
- Novak, G., & Landsberg, R. H., eds. 1998, *Astrophysics from Antarctica*, ASP Conf. Ser. 141 (ASP)
- Penzias, A. A., & Burrus, C. A. 1973, *ARA&A*, 11, 51
- Platt, S. R., Kovac, J., Dragovan, M., Peterson, J. B., & Ruhl, J. E. 1997, *ApJ*, 475, L1
- Radford, S. J. E., Reiland, G., & Shillue, B. 1996, *PASP*, 108, 441
- Ruhl, J. E., Dragovan, M., Platt, S. R., Kovac, J., & Novak, G. 1995, *ApJ*, 453, L1
- Schieder, R., Tolls, V., & Winnewisser, G. 1989, *Exp. Astron.*, 1, 101
- Schwerdtfeger, W. 1984, *Weather and Climate of the Antarctic* (Amsterdam: Elsevier)
- Stark, A. A. 1995, in *Proceedings of Sixth International Symposium on Space Terahertz Technology* (Pasadena: Caltech), 150

- Stark, A. A., Chamberlin, R. A., Cheng, J., Ingalls, J., & Wright, G. 1997, *Rev. Sci. Instr.*, 68, 2200
- Tucker, G. S., Griffin, G. S., Nguyen, H. T., & Peterson, J. S. 1993, *ApJ*, 419, L45
- Ulich, B. L., & Haas, R. W. 1976, *ApJS*, 30, 247
- Walker, C. K., Kooi, J. W., Chan, W., LeDuc, H. G., Schaffer, P. L., Carlstrom, J. E., & Phillips, T. G. 1992, *Int. J. Infrared and Millimeter Waves*, 13, 785
- Waters, J. W. 1976, in *Methods of Experimental Physics: Astrophysics: Part B: Radio Telescopes*, ed. M. L. Meeks, Vol. 12 (New York: Academic Press), 142
- Zhang, X. 1996, *Image and Beam Precession of the AST/RO Telescope*, AST/RO Technical Memorandum 25, AST/RO
- Zmuidzinas, J., & LeDuc, H. G. 1992, *IEEE Trans. Microwave Theory Tech.*, 40, 1797